Dynamical Evolution of Main Belt Meteoroids: Numerical Simulations Incorporating Planetary Perturbations and Yarkovsky Thermal Forces

William F. Bottke, Jr.

Center for Radiophysics and Space Research, Cornell University, Ithaca, New York 14853-6801
E-mail: bottke@astrosun.tn.cornell.edu

David P. Rubincam

Geodynamics Branch, Code 921, Laboratory for Terrestrial Physics, NASA Goddard Space Flight Center, Greenbelt, Maryland 20771

and

Joseph A. Burns

Center for Radiophysics and Space Research, Cornell University, Ithaca, New York 14853-6801

In the Yarkovsky effect, the recoil from asymmetric, reradiated thermal energy causes objects to undergo semimajor axis drift as a function of their spin, orbit, and material properties. We consider the role played by this mechanism in delivering meteoroids from parent bodies in the main belt to chaotic resonance zones where they can be transported to Earth-crossing orbits. Previous work has approximated the dynamical evolution of meteoroids via Yarkovsky forces, mostly through the use of the perturbations equation and simplified dynamics (e.g., Monte Carlo codes). In this paper, we calculate more precise solutions by formulating the seasonal and diurnal variants of this radiation force and incorporating them into an efficient N-body integrator capable of tracking test bodies for tens of millions of years with all relevant planetary perturbations included. Tests of our code against published benchmarks and the perturbation equations verify its accuracy.

Results from long-term numerical integration of meter-sized bodies started from likely meteoroid parent bodies (e.g., 4 Vesta) indicate that dynamical evolution in the inner main belt can be complex. Chaotic effects produced by weaker planetary resonances allow many meteoroids to reach Mars-crossing orbits well before entering the 3 : 1 mean-motion resonance with Jupiter or the ν_6 secular resonance. Outward-evolving meteoroids sometimes become captured in these weaker resonances, increasing e and/or i while a stays constant. Conversely, inward-evolving meteoroids frequently jump across mean-motion resonances with Jupiter, bypassing potential "escape hatches" from the main belt. Despite these effects, our simulations indicate that most stony meteoroids reach Earth-crossing orbits via the 3 : 1 or ν_6 resonance after tens of Myr of evolution in the main belt. These time scales correspond well to the measured cosmic ray exposure ages of chondrites and achondrites. The source of these meteorites, however, is less clear, since Yarkovsky drift allows nearly any body in the main belt to add to the cumulate meteoroid flux. Our results suggest that small parent bodies dominate the meteoroid flux if the main belt size distribution at sub-km sizes is in collisional equilibrium, while big parent bodies dominate if observed population trends for km-sized bodies persist to smaller sizes. © 2000 Academic Press

Key Words: asteroids; asteroids, dynamics; celestial mechanics; meteoroids; meteorites; resonances.

1. INTRODUCTION

During the past several decades, the study of meteorites has opened an increasingly wide window on the nature of extraterrestrial environments, especially conditions in the asteroid belt and early solar nebula. Most meteorites are now believed to be fragments of asteroids that, following ejection in a cratering event on their parent body millions of years ago, wandered through space until they collided with Earth (Marti and Graf 1992). These objects therefore provide very detailed and useful information about asteroid properties and about conditions in the asteroid belt over different epochs.

Unfortunately, we are still struggling to comprehend the provenance, transport, and delivery time scale of meteorites to Earth. One of the most perplexing problems facing meteoriticists is to understand what specific asteroids and/or main belt regions are being sampled via meteorites. Our previous paradigm, that a fragment was blasted off a parent body by a collision and directly injected into a resonance which brought it to Earth, has been recently complicated by the realization that the lifetime

of a body reaching the Earth-crossing (hereafter EC) region via chaotic resonances in the inner main belt is an order of magnitude shorter than previously believed (i.e., roughly a few Myr; Gladman *et al.* 1997). The short dynamical lifetime associated with this delivery scenario is discordant with the longer cosmic-ray exposure (CRE) ages of rocky and iron meteorites (e.g., stones, 10–100 Myr; irons, several 100 Myr–1 Gyr; Caffee *et al.* 1988; Marti and Graf 1992). The classical meteorite delivery scenario also fails to explain why CRE ages for irons are an order of magnitude longer than those for stones.

A plausible way to fix the classical delivery scenario would be to alter the first step; meteoroids, rather than being directly injected into resonances after a collision, would instead reside in the main belt for millions of years before reaching the chaotic resonances which take them to Earth. The inclusion of a transportation mechanism would be needed here, one which could move these objects slowly to resonance so that there would be time for these bodies to collect the appropriate amount of cosmic-ray damage.

We investigate whether this needed transportation mechanism might be Yarkovsky nongravitational forces, a radiation recoil which may cause 0.1- to 100-m objects to undergo semimajor axis drift as a function of their spin, orbit, and material properties. Meteoroids ejected into orbits near the 3 : 1 or ν_6 resonances during cratering events should slowly spiral into those resonances by Yarkovsky drag, giving those objects time to collect cosmic rays before reaching Earth. Recent numerical results indicate that meter-sized stones in the main belt may have drift rates between ±0.01 and 0.001 AU Myr^{-1}, fast enough to allow many parent asteroids to provide material to the 3 : 1 or ν_6 resonances, but slow enough to also explain meteorite CRE ages (Rubincam 1998; Farinella *et al.* 1998a). Irons, with longer collisional lifetimes, may evolve from greater distances, such that they may sample a great proportion of parent bodies in the main belt. For these reasons, we believe an exploration of these thermal forces can potentially allow us to clarify connections between meteorites and their parent bodies in the main belt.

In this paper, we investigate Yarkovsky radiative forces by calculating analytical expressions for their acceleration and incorporating them into a well-tested orbital N-body code ("swift-rmvs3"; Levison and Duncan 1994) capable of simulating the evolution of test bodies anywhere in the inner Solar System. This method allows us, for the first time, to track the evolution of meteoroids all the way from their source bodies to EC orbits (or, with the appropriate parameters, Earth) with all chaotic resonance phenomena included. Our goals for this paper are: (i) to provide the theoretical underpinning for others to include Yarkovsky thermal forces into their own numerical integration codes; (ii) to demonstrate that our Yarkovsky code yields accurate results using direct numerical integration, (iii) to show how the Yarkovsky forces change the orbit of a spinning sphere, and (iv) to apply our code to a problem of interest, specifically the evolution of meteoroids from various parent bodies in the inner main belt.

We have structured the paper as follows. Section 2 discusses the nature of Yarkovsky thermal forces and the previous work that has been accomplished to understand their effect on meteoroids. Section 3 includes our formulation of the diurnal and seasonal Yarkovsky forces. In Section 4, we test our Yarkovsky–Swift model against several benchmarks, those provided by the results of other Yarkovsky simulations and ones coming from the perturbation equations. The dynamical behavior of individual bodies is also discussed here. In Section 5, we show the results for direct, long-term integrations of meteoroids evolving from various parent bodies of interest in the main belt to EC orbits. Transport time scales, dynamical evolution behavior, and phenomena like resonance-jumping and capture are explored. Finally, in Section 6, we discuss the implications of this work while highlighting issues that need to be pursued in the future.

2. YARKOVSKY THERMAL FORCES

2.1. Introduction to the Diurnal and Seasonal Yarkovsky Force Variants

Bodies orbiting the Sun absorb sunlight, mainly in visible wavelengths, and reradiate the energy primarily in infrared wavelengths. When these infrared photons depart, they carry momentum with them, causing the object to recoil slightly. Because thermal inertia delays this kick and the body rotates, the small net force produced by this effect can modify the object's orbit, particularly its semimajor axis. This orbital change is called the Yarkovsky effect, and it is particularly effective among bodies 0.01–100 m in diameter. We refer the reader to Hartmann *et al.* (1999) for a description of how the "Yarkovsky effect" got its name, as well as a summary of several references on this subject (e.g., Peterson 1976; Burns *et al.* 1979; Afonso *et al.* 1995). Note that these forces have been empirically verified in an explanation of the orbital motion of the LAGEOS satellite (Rubincam 1987; Rubincam 1988; Farinella *et al.* 1996; Vokrouhlický and Farinella 1997).

There are two variants of the Yarkovsky effect that work simultaneously (cf. Spitale and Greenberg 1999), a "diurnal" version, which depends on the body's spin rate and longitudinal temperature distribution, and a "seasonal" version, which depends on the body's mean motion around the Sun and its latitudinal temperature distribution. To make this easier to understand, think of the temperature distribution on the Earth. The "diurnal" temperature distribution makes it slightly warmer in the afternoon than at high noon, while the "seasonal" distribution makes the warmest and coldest months come after the summer and winter solstices (e.g., in the Northern Hemisphere, July–August is the hottest period, not June, while January–February is the coldest period, not December).

The diurnal variant is greatest when the spin axis is perpendicular to the orbital plane, and it causes the body to spiral outward for prograde rotations but inward for retrograde rotations. A schematic of force components for an object on a circular orbit
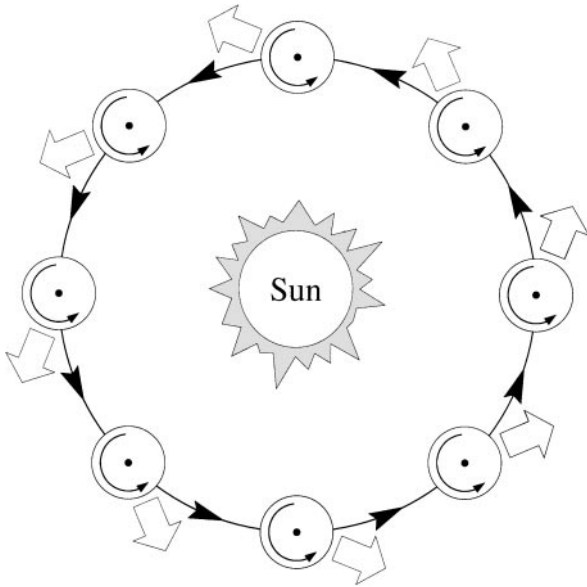
FIG. 1. The diurnal Yarkovsky effect is shown for a rotating body at various places along its circular orbit. The asteroid spin axis is perpendicular to the orbital plane. A fraction of the solar insolation is absorbed only to be later radiated away, yielding a net thermal force in the direction of the wide arrows. Since the thermal reradiation in this prograde-rotation example is concentrated at about 2 PM on the spinning asteroid, the radiation recoil force is always oriented at about 2 AM. In this case, the along-track component causes the object to spiral outward. Retrograde rotation causes the orbit to shrink.

with a prograde rotation is shown in Fig. 1. As will be shown, the effectiveness of the diurnal component varies with the object's rotation rate, such that optimum rotation rates do exist.

The seasonal variant always causes the body to spiral inward, and it is maximum when the object's spin axis lies in the orbital plane. Figure 2 shows a schematic of the forces on an object with its spin pole in the orbital plane. The bottom-most object receives the most asymmetric distribution of solar energy since its spin pole is pointing directly at the Sun. Energy is reradiated here, causing a kick in the anti-Sun direction, but, because of thermal inertia, the maximum reradiation does not occur until later in the orbit. Thus, as Fig. 2 shows, the seasonal Yarkovsky force averaged over the orbit opposes the orbital motion and does work. The net effect is to cause the orbit to shrink in size, regardless of the rotation speed of the object. Thus, we get thermal drag for all spin axis orientations.

2.2. Previous Work

Several recent papers (e.g., Rubincam 1995; 1998; Farinella *et al.* 1998a; Vokrouhlický 1998a; Vokrouhlický 1999) have examined how the Yarkovsky effect modifies the orbit of a spherical solid body. Using complementary (linear) formulations of the temperature distribution for a rotating body illuminated by the Sun, they calculated average drift rates for various meteoroid sizes and properties which agree with one another. We use their results as benchmarks for the Yarkovsky formulation presented

below. Related work exploring the effects of nonlinear thermal models (Vokrouhlický and Farinella 1998a) and nonspherical meteoroids (Vokrouhlický 1998b) indicate that the above formulations yield satisfactory results for most problems of interest. Numerical finite-element models (Spitale and Greenberg 1999) demonstrate that the Yarkovsky effect cannot be decomposed for diurnal and seasonal variants at high eccentricity.

The next progressive step in producing a realistic simulation is to incorporate Yarkovsky forces in conjunction with resonant N-body dynamics. The cumulate gravitational effects of the jovian and terrestrial inner planets make the orbital paths of meteoroids strongly chaotic, with the inner Solar System crisscrossed by mean-motion and secular resonances. When main-belt-asteroid fragments become trapped in resonant locations like the 3 : 1 mean-motion resonance with Jupiter or the ν_6 secular resonance, their orbits become strongly perturbed and can be driven to high eccentricities and inclinations (Gladman *et al.* 1997). Indeed, these objects frequently reach EC orbits or even Sun-grazing orbits (Farinella *et al.* 1994).

These effects are impossible to fully reproduce analytically, but approximate methods can yield suggestive results. To this end, Vokrouhlický and Farinella (1998b) combined the seasonal Yarkovsky drift rate with a semianalytic method for estimating
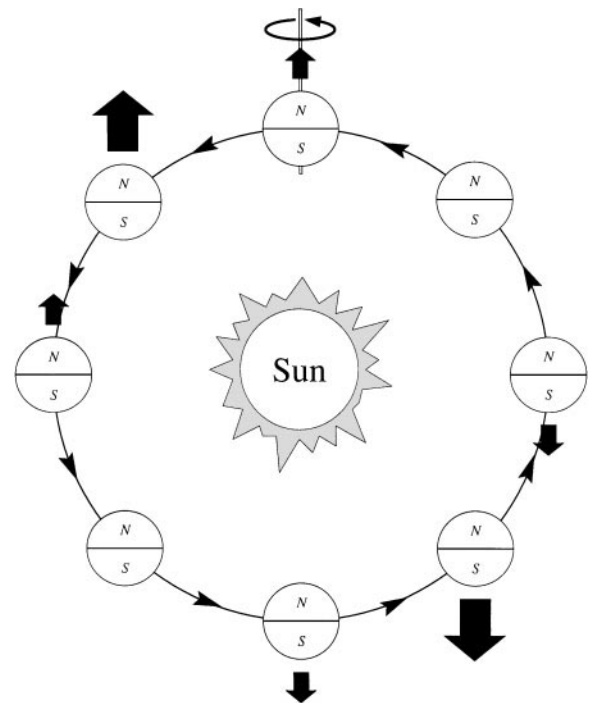
FIG. 2. The seasonal Yarkovsky effect at various points along a circular orbit for an asteroid whose spin axis lies in the orbital plane as shown at the top of the figure. Seasonal heating and cooling of the "northern" and "southern" hemispheres give rise to a thermal force which lies along the spin axis. The strength of the reradiation force varies along the orbit as a result of thermal inertia; the maximum resultant radiative forces are applied to the body somewhat after their most asymmetric (N vs S) energy absorption has occurred. The net effect over one revolution always causes the object to spiral inward.

the average gravitational perturbing function for a main-belt meteoroid, allowing them to numerically integrate its corresponding system of Lagrange's equations. Their goal was to track the orbital paths of bodies started on circular orbits between 2.1 and 2.3 AU to the ν_6 secular resonance. They found that 5- to 10-m objects with basaltic surface properties drift into the ν_6 resonance after several tens of Myr of evolution (on average). The inclusion of secular perturbations in their model was found to induce small oscillations in eccentricity as the meteoroid moved inward. They observed few inclination changes en route, though they claimed this was probably a consequence of some simplifying assumptions. Once their objects entered the ν_6 resonance, the es and is were pumped up to maximum values of 0.6–0.7 and $10°$–$15°$, respectively. These upper limits were by-products of their semianalytic method. They noted that the Yarkovsky seasonal drag did not seriously affect the object once it entered the ν_6 resonance.

The model we describe below is a continuation of the progress these groups have made in realistically modeling meteoroid evolution. The next section shows how we calculate the diurnal and seasonal Yarkovsky forces at any given point in a meteoroid's orbit, while the following sections describe the many diagnostic tests we used to verify that our model was working correctly.

3. NUMERICALLY MODELING THE YARKOVSKY EFFECT

To model the evolution of meteoroids accurately, we first formulated the diurnal and seasonal Yarkovsky drag accelerations, which are functions of many parameters, the object's size, spin rate, spin axis orientation, material properties, and its distance from the Sun (Section 3.1). Next, we included these accelerations into a numerical orbital integration routine (Section 3.2). After testing, we introduced a few related modifications (e.g., collisions) into the code to make the meteoroid evolution simulations more realistic (Section 4.5).

3.1. Formulation of Diurnal and Seasonal Yarkovsky Accelerations

3.1.1. Magnitude of the force. In order to establish notation, correct minor previous errors, and tell a coherent story, we have rederived useful parts of the Yarkovsky formalism below.

Assuming Lambert's law (e.g., Peterson 1976), the force from any given surface element dA on a thermally radiating body is

$$\frac{dp}{dt} = \left(\frac{2\epsilon\sigma}{3c}\right)T^4 \, dA, \qquad (1)$$

where p is momentum, ϵ is the emissivity, σ is the Stefan–Boltzmann constant, T is the temperature, and c is the speed of light. The direction of the force $\hat{n}$ is normal to the surface element, i.e., parallel to dA, which for a sphere is

$$\hat{n} = (\sin\theta\cos\lambda)\hat{x} + (\sin\theta\sin\lambda)\hat{y} + (\cos\theta)\hat{z}, \qquad (2)$$

where θ is the colatitude measured on the body from its spin

axis orientation $\hat{b}$ (which also defines the z axis), λ is the east longitude measured on the body from an arbitrarily oriented x axis, and x, y, z are fixed to the body. For these body-centered coordinates, x and y are in the body's equatorial plane, with x, y, z defining a right-handed system.

The direction of $\hat{n}$ can also be written in terms of the unnormalized spherical harmonic $Y_{lmn}(\theta, \lambda)$, where l is the degree, m is the order, and n is cosine ($n = 1$) or sine ($n = 2$) spherical harmonics. Thus, $Y_{lm1}(\theta, \lambda) = P_{lm}(\cos\theta)\cos(m\lambda)$, while $Y_{lm2}(\theta, \lambda) = P_{lm}(\cos\theta)\sin(m\lambda)$, where $P_{ml}(\cos\theta)$ is the associated Legendre polynomial. For first-degree terms, $Y_{111}(\theta, \lambda) = \sin\theta\cos\lambda$, $Y_{112}(\theta, \lambda) = \sin\theta\sin\lambda$, and $Y_{101}(\theta, \lambda) = \cos\theta$. These definitions will be used below.

Expanding the temperature in a Taylor series as

$$T^4 \approx T_0^4\left(1 + \frac{4\Delta T}{T_0}\right) = T_0^4 + 4T_0^3\Delta T \qquad (3)$$

yields for the varying point of the acceleration

$$\frac{dp}{dt} \approx \frac{8\epsilon\sigma}{3c}T_0^3\Delta T \, dA. \qquad (4)$$

Here T_0 is a constant throughout the asteroid, and it is related to the body's average insolation by (Rubincam 1998)

$$T_0 = \left\{\frac{(1-A)}{4\sqrt{1-e^2}\epsilon\sigma}F_\oplus\left(\frac{1\,\text{AU}}{a}\right)^2\right\}^{1/4}, \qquad (5)$$

where a is the body's semimajor axis, e is the orbit's eccentricity, A is albedo, and the insolation $F_\oplus = 1378$ W m^{-2}. If we expand ΔT as a sum of spherical harmonics,

$$\Delta T = \sum_{m,n} \Delta T_{1mn}Y_{1mn}(\theta, \lambda), \qquad (6)$$

keeping only the first-degree terms,

$$\Delta T = \Delta T_{111}Y_{111}(\theta, \lambda) + \Delta T_{112}Y_{112}(\theta, \lambda) + \Delta T_{101}Y_{101}(\theta, \lambda) \qquad (7)$$

with ΔT_{111}, ΔT_{112}, and ΔT_{101} as time-dependent numerical coefficients, and we assume the body is a sphere, we can integrate the "force" over the body's surface in each direction. The first-degree acceleration components can then be written

$$x\text{ accel.} = \left(\frac{8\epsilon\sigma T_0^3}{3c\rho R}\right)\Delta T_{111} \qquad (8)$$

$$y\text{ accel.} = \left(\frac{8\epsilon\sigma T_0^3}{3c\rho R}\right)\Delta T_{112} \qquad (9)$$

$$z\text{ accel.} = \left(\frac{8\epsilon\sigma T_0^3}{3c\rho R}\right)\Delta T_{101}, \qquad (10)$$

where R and ρ are the body's radius and density.

3.1.2. Temperature variation over the body.

To estimate the first-degree temperature variation ΔT, we use a linearized thermal model (with spherical Bessel functions) to solve the heat conduction equation when $r = R$ (Rubincam 1998),

$$K\frac{\partial \Delta T}{\partial r} + 4\epsilon\sigma T_0^3 \Delta T = (1 - A)\,\Delta F, \qquad (11)$$

where ΔF is the first-degree insolation,

$$\Delta F = \frac{1}{2}F_{\oplus}\left(\frac{1\,\text{AU}}{r_s}\right)^2 [\hat{n} \cdot (-\hat{r}_s)], \qquad (12)$$

where $-\mathbf{r_s}$ is the vector from the body to the Sun defined in heliocentric–ecliptic coordinates:

$$-\mathbf{r_s} = -r_s[(\sin\theta_s \cos\lambda_s)\hat{x}_s + (\sin\theta_s \sin\lambda_s)\hat{y}_s + (\cos\theta_s)\hat{z}_s]. \qquad (13)$$

Here, $\hat{x}_s$ is the direction of the vernal equinox, $\hat{z}_s$ is the direction normal to the ecliptic plane, and $\hat{y}_s$ is chosen to form a right-handed set of coordinates; θ_s and λ_s are the colatitude and east longitude of the Sun in the x_s, y_s, z_s system.

We can rewrite ΔF as a sum of spherical harmonics (in body and heliocentric–ecliptic coordinates),

$$\Delta F = \sum_{m,n} \Delta F_{1mn} Y_{1mn}(\theta, \lambda), \qquad (14)$$

and

$$\Delta F = \frac{1}{2}F_{\oplus}\left(\frac{1\,\text{AU}}{r_s}\right)^2 [Y_{111}(\theta_s, \lambda_s)Y_{111}(\theta, \lambda) + Y_{112}(\theta_s, \lambda_s)Y_{112}(\theta, \lambda) + Y_{101}(\theta_s, \lambda_s)Y_{101}(\theta, \lambda)]. \qquad (15)$$

The time dependence is contained implicitly in θ_s and λ_s.

We will assume each insolation coefficient ΔF_{1mn} has the general form

$$\Delta F_{1mn} = \Delta F_{1mn}^0 e^{i\nu t}, \qquad (16)$$

where $\nu = \omega$, the spin frequency appropriate for the diurnal effect, or $\nu = n$, the orbital frequency appropriate for the seasonal effect, t is the time, and ΔF_{1mn}^0 is time-independent. In the case of a circular orbit, ν always combines the rotation and revolution frequencies (e.g., $(\omega \pm n)$; Vokrouhlický 1999). Similarly, we can express the temperature coefficients ΔT_{1mn} as

$$\Delta T_{1mn} = \tau_{1mn}^0 j_1(kr)e^{i\nu t}, \qquad (17)$$

where τ_{1mn}^0 is a constant, r is the radial distance from the center of the asteroid, and $j_1(kr)$ is the spherical Bessel function,

$$j_1(kr) = \frac{\sin(kr)}{(kr)^2} - \frac{\cos(kr)}{kr}, \qquad (18)$$

and

$$k = \left(\frac{-i\nu\rho C_p}{K}\right)^{1/2}. \qquad (19)$$

Substituting (18) and (19) into (17), we can solve for τ_{1mn}^0,

$$\tau_{1mn}^0 = \frac{(1 - A)\Delta F_{1mn}R}{K}\left[\frac{z^2}{c_1 z \cos z - c_1 \sin z + z^2 \sin z}\right] \qquad (20)$$

with

$$z = kR = x(1 - i) \qquad (21)$$

$$x = R\left(\frac{\nu\rho C_p}{2K}\right)^{1/2}, \qquad (22)$$

and

$$c_1 = 2\left(1 - \frac{2\epsilon\sigma T_0^3 R}{K}\right). \qquad (23)$$

The real and imaginary parts of the complex numbers of (20), when multiplied by $j_1(z)$, can be written as (Rubincam 1998)

$$\frac{z^2 j_1(z)}{c_1 z \cos z - c_1 \sin z + z^2 \sin z} = \frac{C_1 - iC_2}{C_3}, \qquad (24)$$

where

$$C_1 = 2x(c_1 + x^2)\sinh 2x + 2x(c_1 - x^2)\sin 2x - c_1(1 + 2x^2)\cosh 2x + c_1(1 - 2x^2)\cos 2x \qquad (25)$$

$$C_2 = 2x^2(x\sinh 2x + x\sin 2x + \cos 2x - \cosh 2x) \qquad (26)$$

$$C_3 = \left[c_1^2(1 + 2x^2) + 4x^4\right]\cosh 2x + \left[c_1^2(-1 + 2x^2) - 4x^4\right]\cos 2x - 2c_1 x(c_1 + 2x^2)\sinh 2x - 2c_1 x(c_1 - 2x^2)\sin 2x. \qquad (27)$$

We will express $\tau_{1mn}^0 j_1(z)$ in the complex form "magnitude" $\times$ $\exp(-i \times$ "lag angle"), which makes the surface temperature
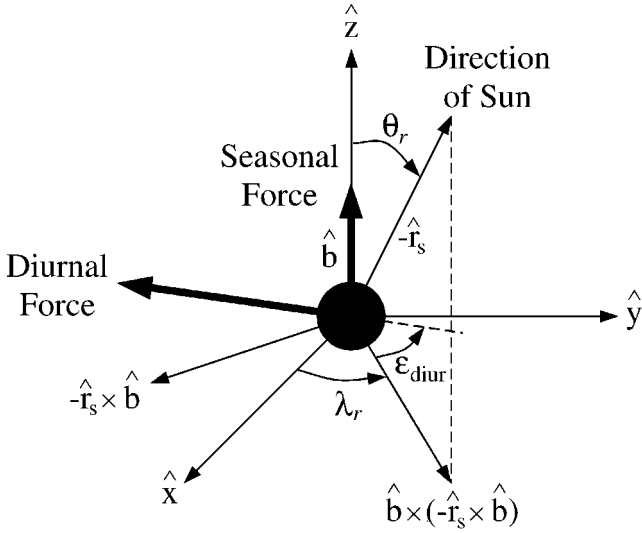
$$\Delta T_{1mn} = \Delta T_{1mn}^0 e^{i(\nu t - \delta)} \qquad (28)$$

with ΔT_{1mn}^0 being the time-independent amplitude,

$$\Delta T_{1mn} = \frac{(1 - A)\Delta F_{1mn}R}{K}\left(\frac{C_1^2 + C_2^2}{C_3^2}\right)^{1/2}, \qquad (29)$$

and δ being the lag angle,

$$\delta = \arcsin\left(\frac{C_2}{\sqrt{C_1^2 + C_2^2}}\right). \qquad (30)$$

FIG. 3. Geometry for the Yarkovsky effect. Here, $-\hat{r}_s$ is the unit vector pointing toward the Sun while $\hat{b}$ is the body's spin axis orientation. Using body-centered coordinates, $\hat{z}$ is defined to be in the $\hat{b}$ direction, while $\hat{x}$ and $\hat{y}$ are defined to form a right-handed set of coordinates in the body's equatorial plane. Also, θ_r is the colatitude for $-\hat{r}_s$, λ_r is the east longitude measured between $\hat{x}$ and the projection of $-\hat{r}_s$ in the x, y plane, and $\varepsilon_{\text{diur}}$ is the lag angle for the diurnal force. The diurnal force acts in the opposite direction from the dashed vector projected from $\varepsilon_{\text{diur}}$. The seasonal force acts along $\hat{b}$.

3.1.3. Diurnal Yarkovsky acceleration. Using (28), we can substitute back into (8)–(10) to get the Yarkovsky accelerations. Here we consider the diurnal Yarkovsky acceleration, which is a function of the longitudinal temperature distribution.

To find the diurnal acceleration, it is useful to define $-\mathbf{r}_s$ in body-centered coordinates (i.e., $\hat{b}$ defines the z axis):

$$-\mathbf{r_s} = -r_s[(\sin\theta_r \cos\lambda_r)\hat{x} + (\sin\theta_r \sin\lambda_r)\hat{y} + (\cos\theta_r)\hat{z}]. \quad (31)$$

This equation is similar to Eq. (2) except θ_r and λ_r are referenced to $-\hat{r}_s$ rather than $\hat{n}$. The geometry is shown in Fig. 3.

The time dependence of the diurnal force will come from the longitude λ_r as seen from the meteoroid (i.e., $\lambda_r = -\omega t$, where ω is the meteoroid's rotation rate). It rotates in the positive sense as seen from inertial space. As seen from an observer on the meteoroid, the Sun rotates in the negative sense, accounting for the minus sign. Thus, the force in the body-centered x, y directions will lag the Sun,

$$Y_{111}(\theta_r, \lambda_r)|_{\text{lagged}} \rightarrow \sin\theta_r \cos(\lambda_r + \varepsilon_{\text{diur}}) \quad (32)$$

$$Y_{112}(\theta_r, \lambda_r)|_{\text{lagged}} \rightarrow \sin\theta_r \sin(\lambda_r + \varepsilon_{\text{diur}}), \quad (33)$$

where the lag angle for the diurnal force $\delta = \varepsilon_{\text{diur}}$. Note that $\varepsilon_{\text{diur}}$ is a positive angle, and we write $\lambda_r + \varepsilon_{\text{diur}}$ rather than $\lambda_r - \varepsilon_{\text{diur}}$ to get the proper sign of the lag (i.e., $\lambda_r = -\omega t$). This assumes that $\omega \gg n$, thus decoupling the rotation from the position of the meteoroid in its orbit so that colatitude θ_r and distance to the Sun, r_s, are not lagged in the force equation below.

To get the force direction, we create a right-handed coordinate system referenced to the these body-centered coordinates, with the new x-axis ($\hat{x}_f$) defined by $-\hat{r}_s \times \hat{b}$ and the new y-axis ($\hat{y}_f$) defined by $\hat{b} \times (-\hat{r}_s \times \hat{b})$, which is the projection of $-\hat{r}_s$ in the x, y plane (Fig. 3). This coordinate system was chosen to keep the $\hat{y}_f$ axis pointing (more or less) at the Sun, with $\varepsilon_{\text{diur}}$ measured in the counterclockwise direction.

From geometry, the diurnal Yarkovsky force can then be written

$$\ddot{\mathbf{r}}_{\text{diur}} = C_{\text{diur}} F_{\oplus}\left(\frac{1 \text{ AU}}{r_s}\right)^2 [\sin\varepsilon_{\text{diur}}(\hat{b} \times \hat{r}_s)$$
$$+ \cos\varepsilon_{\text{diur}}(\hat{b} \times (\hat{r}_s \times \hat{b}))] \quad (34)$$

with C_{diur} being the amplitude appropriate for the diurnal effect (i.e., we use $\nu = \omega$ when solving for C_1, C_2, C_3).

$$C_{\text{diur}} = \frac{4(1-A)\epsilon\sigma T_0^3 R}{3Kc\rho}\left(\frac{C_1^2 + C_2^2}{C_3^2}\right)^{1/2} \quad (35)$$

From this point on, $\hat{b}$ and $\hat{r}_s$ will be expressed in heliocentric–ecliptic coordinates rather than body-centered coordinates.

Note that Eq. (34) uses the average equilibrium temperature (T_0) of the meteoroid over one revolution rather than the local equilibrium temperature defined at each point along the orbit. The former value is valid for low eccentricity orbits, while the latter value is more general (e.g., Vokrouhlický 1998a, Rubincam 1998). Since the numerical tests described in Sections 4 and 5 concentrate on low-e meteoroids, our approximation yields accurate results.

3.1.4. Seasonal Yarkovsky acceleration. The seasonal Yarkovsky force is similar to the diurnal Yarkovsky force, except it is a function of the latitudinal temperature distribution

$$\ddot{\mathbf{r}}_{\text{sea}} = C_{\text{sea}} F_{\oplus}(1 \text{ AU})^2\left[\frac{(\hat{b} \cdot \hat{r}_s)}{r_s^2}\right]_{\text{lag}} \hat{b}, \quad (36)$$

where C_{sea} is the same as C_{diur} except that the orbital frequency $\nu = n$ is now used when solving for C_1, C_2, C_3. "Lag" means this quantity at some earlier time, the time interval between now and then being fixed. The seasonal force, however, operates along the present spin axis.

The time delay between the "lagged" force and the meteoroid's current position is

$$t_{\text{lag}} \approx \frac{\varepsilon_{\text{sea}}}{n}, \quad (37)$$

where n is the body's mean-motion. We can find ε_{sea} from (30) using $\omega = n$. Note that this method is most accurate for low-e orbits, where a single orbit-averaged t_{lag} value can approximate the change in seasonal acceleration as the meteoroid passes between perihelion and aphelion.

### 3.2. Inclusion of Yarkovsky Accelerations into Orbital Evolution Code

We incorporated the Yarkovsky accelerations into the "swift-rmvs3" numerical integrator designed by Levison and Duncan (1994) and based on the symplectic formulation proposed by Wisdom and Holman (1991). This is possible because the drift accelerations above are not velocity-dependent, allowing us to preserve the attributes of the symplectic integration technique. Note that even though swift-rmvs3 is not technically symplectic (i.e., it lowers the integration time step when treating planetary close encounters), it does handle highly eccentric orbits efficiently enough to make it much faster than any other numerical integration code publicly available. Additional information on the statistical accuracy of this code is available from Michel and Valsecchi (1996) and Duncan and Lissauer (1997).

The Yarkovsky acceleration components are calculated at each integration time step, which is always a small fraction of the test body's orbital period. The seasonal acceleration, however, is complicated to calculate, since the magnitude of the force depends on distance and spin axis parameters from previous time steps (i.e., through ΔT, which is a function of the incident solar flux) and not, like the usual drag forces, on the instantaneous position and/or velocity. To deal with this, position parameters are stored in an array at each time step for later use. By estimating t_{lag}, we can interpolate between saved positions to estimate the lag values of $\mathbf{r_s}$. A more accurate method would involve solving Kepler's equation at each time step, but the computational time penalty would be prohibitive. We have found that linear interpolation schemes using Cartesian and polar coordinates yield similar results, though the latter are more appropriate for elliptical orbits.

4. TESTING THE YARKOVSKY-SWIFT-RMVS3 (YS) CODE

4.1. Effect of Yarkovsky Forces on Semimajor Axis

To verify that our code was running correctly, we performed validity tests against the benchmark da/dt drift rate results produced by Rubincam (1995, 1998) and Farinella et al. (1998a). We focus on the Farinella et al. benchmark tests below, since the method discussed in Section 3 is closely related to Rubincam (1995, 1998). Test bodies in the "Yarkovsky-swift-rmvs3" (YS) code were given the following thermal and material properties: thermal conductivity $K = 2.65$ W m^{-1} K^{-1}, specific heat $C_p = 680$ J kg^{-1} K^{-1}, bulk density $\rho = 3500$ kg m^{-3}, emissivity $\epsilon = 1.00$, and albedo $A = 0.0$. The spin periods were either set to $P = 5$ h, corresponding to the median value of small asteroids (Harris 1996), or $P = 5$ h $\times (2R/1$ km), corresponding to the spin rates of fragments measured in laboratory impacts experiments (e.g., Farinella et al. 1998a), which were extrapolated to larger sizes. Given that 1998 KY26, a 30-m EC asteroid, has a spin period of ~ 10 min (Ostro et al. 1999), we believe the latter estimate is more likely to apply to meteoroids.
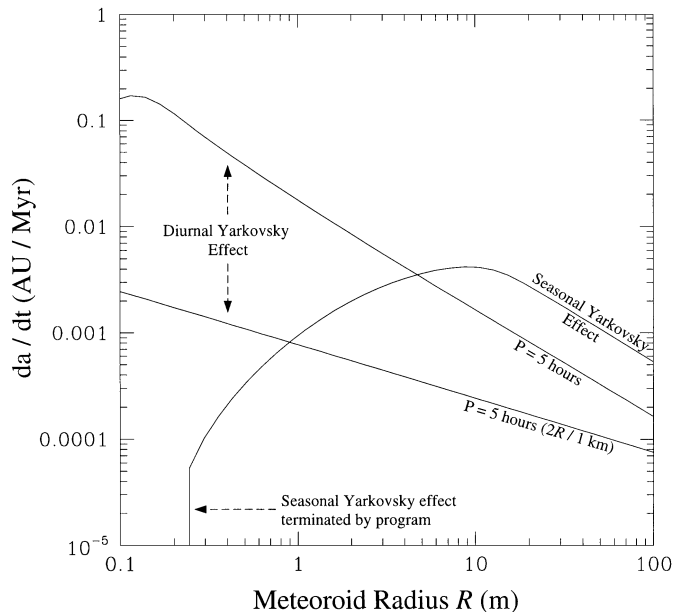

FIG. 4. Maximum diurnal and seasonal mean drift rates (i.e., averaged over one revolution) for variously sized meteoroids on initially circular orbits with semimajor axes $a = 2$ AU. For the diurnal runs, the spin axis orientations of the bodies ($\hat{b}$) were set to (0.0, 0.0, -1.0) in heliocentric–ecliptic coordinates. Their rotation periods P are indicated. The seasonal runs had $\hat{b} = (0.0, 1.0, 0.0)$. Other parameters used for these runs include thermal conductivity $K = 2.65$ W m^{-1} K^{-1}, specific heat $C_p = 680$ J kg^{-1} K^{-1}, density $\rho = 3500$ kg m^{-3}, emissivity $\epsilon = 1.00$, and albedo $A = 0.0$. These runs agree with Farinella et al. (1998a), provided a neglected factor of 2 multiplies their seasonal rates (Farinella et al. 1998b).

Figure 4 shows the maximum diurnal and seasonal da/dt drift rates (averaged over one revolution) for variously sized meteoroids on initially circular orbits with semimajor axes $a = 2$ AU. No planets were included in these runs. The integration time step was 30 days. To get the maximum diurnal drift rate, the spin axis was oriented perpendicular to the orbital plane (i.e., using heliocentric–ecliptic coordinates, $\hat{b} = 0.0, 0.0, -1.0$). Similarly, the maximized seasonal drift rate, $\hat{b}$, was placed in the orbit plane ($\hat{b} = 0.0, 1.0, 0.0$). The drift rate was found by integrating the bodies for 1 Myr and subtracting the initial and final a values.

Our results match Fig. 1 of Farinella et al. (1998a) once an erroneous factor of 1/2 is removed from the their seasonal drag rates (Farinella et al. 1998b). Small meteoroids have the fastest diurnal da/dt rates, though the magnitudes of these values decrease with increasing spin rate. Seasonal da/dt rates peak near $R = 10$ m ($da/dt \sim -0.004$ AU Myr^{-1}). The magnitudes of the seasonal and diurnal da/dt rates for $R \sim 1$ m bodies are roughly the same; $\hat{b}$ determines whether these effects constructively or destructively interfere. (Note that we turn off the seasonal effect for $R < 20$ cm bodies to avoid computational round-off errors in our coded version of Section 3.1.2. Since the dynamical evolution of such small bodies is beyond the scope of this paper, we ignore this minor problem at this time).

Figure 5 shows the maximum seasonal da/dt rates for meteoroids on circular orbits with semimajor axes $a = 1, 2$, and
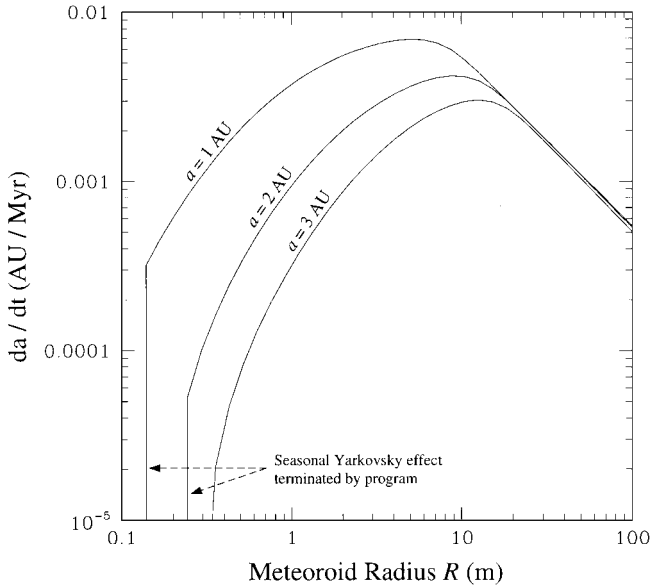
FIG. 5. Seasonal Yarkovsky drift rates for variously sized meteoroids on initially circular orbits with semimajor axes $a = 1, 2, 3$ AU. The $\hat{b}$ values were set to (0.0, 1.0, 0.0), which provides maximum seasonal drift rates. Other parameters are given in the caption to Fig. 4. These results agree with Farinella *et al.* (1998a), provided their seasonal rates are multiplied by a neglected factor of 2.

3 AU. Once again, our plot matches Fig. 2 of Farinella *et al.* (1998a) after a factor of $1/2$ is removed from their results. We find that seasonal drag rates for $R > 20$ m bodies nearly converge for $a = 1, 2,$ and 3 AU. This behavior is similar to that seen in Fig. 5 of Rubincam (1998); basaltic objects with $R = 10$ m have nearly constant da/dt rates between 0.4 and 3.0 AU.

We can explain this result using proportionality relationships. Assuming our large meteoroids travel on circular orbits, $da/dt \propto S/n$, where S is the along-track acceleration (with thermal lag terms included). Since S is proportional to solar flux, which changes like $\propto a^{-2}$, and $n \propto a^{-3/2}$, $da/dt \propto a^{-1/2}$, a fairly slow rate. (Note that we are ignoring da/dt's dependence on meteoroid size at this time.) When factors like asteroid rotation (and thermal lag) are included, we get a nearly constant da/dt rate for nearly any distance between Mercury and the main belt. Another way of describing this effect is that, for large bodies, the thermal wave produced by absorbed sunlight largely fails to reach the other side of the meteoroid. Accordingly, we can treat these bodies like infinite half-spaces, such that their thermal properties are independent of R (Burns *et al.* 1979, Rubincam 1995). This approximation yields an R^{-1} force dependence (i.e., the area of the meteoroid exposed to sunlight, $\propto R^2$, divided by its mass, $\propto R^3$), explaining the straight lines seen on the right side of our Fig. 5.

4.2. Effect of Yarkovsky Forces on Eccentricity and Inclination

4.2.1. Results from numerical simulations. We now examine how a meteoroid's eccentricity and inclination are modified by Yarkovsky accelerations. Our intuition on how meteoroids should evolve is limited by the complexity of the system (pa-

rameters a, e, i; spin axis orientation b_x, b_y, b_z; and both seasonal and diurnal Yarkovsky accelerations). For this reason, we have chosen to investigate a series of simple test cases before addressing more complicated behavior. Unusual results will be discussed in Section 4.3.

The test meteoroid was an $R = 1$ m body with the same material and thermal properties described previously. The length of our integrations was 1 Myr. Seasonal and diurnal Yarkovsky accelerations were tested separately, and orbital changes caused solely by diurnal accelerations ($\Delta a_{\text{diur}}, \Delta e_{\text{diur}}, \Delta i_{\text{diur}}$) and seasonal accelerations ($\Delta a_{\text{sea}}, \Delta e_{\text{sea}}, \Delta i_{\text{sea}}$) are indicated in Table I. For the runs shown there, $\hat{b}$ was placed in a variety of directions; some in the orbital plane ($b_z = 0$), some normal to the orbital plane ($b_x, b_y = 0$), and some at a 45° angle to the orbital plane.

The first 14 test cases have the test body on a circular orbit in the ecliptic plane ($a = 2$ AU, $e = 0.0$, and $i = 0°$). Recall that no planets are included in these runs. For the first 6 runs (spin axis orientation $\hat{b} = \pm\hat{x}_s, \pm\hat{y}_s,$ and $\pm\hat{z}_s$), we see no e changes. Small i changes ($\pm0.0055°$) were caused by the diurnal effect when $\hat{b}$ was in the x_s, y_s plane. The next 8 cases ($\hat{b}$ at a 45° angle to the x_s, y_s plane) show Δa_{diur} and Δa_{sea} with nearly the same magnitude. Accordingly, the sign of $\hat{b}$ determines whether da/dt doubles or nearly cancels out. No de/dt changes are seen but, surprisingly, Δi_{sea} is found to be nearly 1° per Myr, large enough to drive inner main belt stony meteoroids to high inclinations (and into the ν_6 resonance) within their expected disruption lifetimes. This high rate will be examined in closer detail in the next section, particularly when more realistic orbital behavior (e.g., orbital precession of the apsides and nodes caused by secular perturbations) is included.

The second 14 cases used a meteoroid on an initially eccentric orbit (i.e., $a = 2$ AU, $e = 0.3$, and $i = 0°$). The increased magnitude of the Yarkovsky accelerations when the object is closer to the Sun (near perihelion) is balanced to some degree by the greater amount of time the object spends far from the Sun (near aphelion). Accordingly, the magnitude of Δa and Δi increases slightly for the second 14 cases compared to the comparable first 14 cases. Note that the seasonal accelerations tend to circularize the orbit, and that Δe_{sea} is the most negative when $\hat{b}$ is in the orbital plane.

We have also examined the effect of inclination changes, but, without planetary perturbations, they produce the same $\Delta a, \Delta e,$ and Δi results as when $\hat{b}$ is directed out of the orbital plane. For example, a circular orbit with $i = 90°$ and $\hat{b}_z = 1.0$ is equivalent to $i = 0°$ and $\hat{b}_z = 0.0$. This makes sense, since thermal forces are dependent on the specific characteristics of the meteoroid and its distance from the Sun, not how far it lies above or below an arbitrarily defined plane. Hence, the salient parameter is $\hat{b}$'s orientation (obliquity) relative to the meteoroid's orbital plane.

A final inspection of Table I shows that the diurnal acceleration noticeably modifies a and i while the seasonal acceleration modifies a, e, i. Diurnal changes to i and seasonal changes to e occur so slowly, however, that they are unimportant for questions

TABLE I
Orbital Changes to an $R = 1$ m Meteoroid via the Yarkovsky Effect

a (AU)	e	i (deg)	$\hat{b}_x$	$\hat{b}_y$	$\hat{b}_z$	Δa_{diur} (10^{-3} AU)	Δe_{diur} (10^{-3})	Δi_{diur} (10^{-3} deg)	Δa_{sea} (10^{-3} AU)	Δe_{sea} (10^{-3})	Δi_{sea} (10^{-3} deg)
2.0	0.0	0.0	1.0	0.0	0.0	0.00	0.00	5.5	−0.94	0.0	0.0
			−1.0	0.0	0.0	0.00	0.00	5.5	−0.94	0.0	0.0
			0.0	1.0	0.0	0.00	0.00	5.5	−1.0	0.0	0.0
			0.0	−1.0	0.0	0.00	0.00	5.5	−1.0	0.0	0.0
			0.0	0.0	1.0	0.77	0.00	0.0	0.0	0.0	0.0
			0.0	0.0	−1.0	−0.77	0.00	0.0	0.0	0.0	0.0
			0.7	0.0	0.7	0.54	0.00	0.48	−0.47	0.0	930.0
			−0.7	0.0	0.7	0.54	0.00	0.48	−0.47	0.0	930.0
			0.7	0.0	−0.7	−0.54	0.00	0.48	−0.47	0.0	930.0
			−0.7	0.0	−0.7	−0.54	0.00	0.48	−0.47	0.0	930.0
			0.0	0.7	0.7	0.54	0.00	0.48	−0.52	0.0	930.0
			0.0	−0.7	0.7	0.54	0.00	0.48	−0.52	0.0	930.0
			0.0	0.7	−0.7	−0.54	0.00	0.48	−0.52	0.0	930.0
			0.0	−0.7	−0.7	−0.54	0.00	0.48	−0.52	0.0	930.0
2.0	0.3	0.0	1.0	0.0	0.0	0.00	0.00	5.9	−1.3	−0.15	0.0
			−1.0	0.0	0.0	0.00	0.00	5.9	−1.3	−0.15	0.0
			0.0	1.0	0.0	0.00	0.00	6.2	−1.3	−0.09	0.0
			0.0	−1.0	0.0	0.00	0.00	6.2	−1.3	−0.09	0.0
			0.0	0.0	1.0	0.88	0.00	0.0	0.0	0.0	0.0
			0.0	0.0	−1.0	−0.88	0.00	0.0	0.0	0.0	0.0
			0.7	0.0	0.7	0.62	0.00	5.1	−0.66	0.0	1000.0
			−0.7	0.0	0.7	0.62	0.00	5.1	−0.66	0.0	1000.0
			0.7	0.0	−0.7	−0.62	0.00	5.1	−0.66	0.0	1000.0
			−0.7	0.0	−0.7	−0.62	0.00	5.1	−0.66	0.0	1000.0
			0.0	0.7	0.7	0.62	0.00	5.1	−0.65	0.0	970.0
			0.0	−0.7	0.7	0.62	0.00	5.1	−0.65	0.0	970.0
			0.0	0.7	−0.7	−0.62	0.00	5.3	−0.65	0.0	970.0
			0.0	−0.7	−0.7	−0.62	0.00	5.3	−0.65	0.0	970.0

Note. The first three columns list the starting orbit, while the next three columns show the meteoroid's spin axis orientation in heliocentric–ecliptic coordinates. The last six columns describe orbital variations caused by the diurnal (d) and seasonal (s) accelerations over 1 Myr. Thermal conductivity is for bare basalt ($K = 2.65$ W m^{-1} K^{-1}). Other meteoroid properties are described in the text.

of meteoroid delivery. Seasonal i changes, though, are interesting enough to merit additional study.

4.2.2. Discussion of inclination changes produced by seasonal Yarkovsky acceleration. Table I shows that the seasonal Yarkovsky acceleration causes nonnegligible i changes to meteoroid orbits when their spin axes are neither parallel nor perpendicular to their orbit plane. To explore this result further, we tested da/dt and di/dt rate changes for differently sized meteoroids when $\hat{b}$ was pointing at a 45° angle out of the orbital plane; $\hat{b} = (0.707, 0.0, 0.707)$. The meteoroids were assumed to have orbital parameters $a = 2.0$ AU, $e = 0.0$, and $i = 0°$ and the same physical and thermal properties as the test meteoroids described above. No planets were included in our integrations.

The da/dt results for our new test cases are a factor of 2 lower in magnitude than the seasonal acceleration results shown in Fig. 4, though they keep the same maximum (i.e., near $R \sim 10$ m) and parabolic shape. Surprisingly, though, di/dt values do not follow this parabolic trend; rather, they increase as R decreases (Fig. 6). Note that di/dt is nearly flat for $R < 0.1$ m but drops off linearly for $R > 10$ m. No da/dt-like turnover is seen near

$R \sim 10$ m. These results suggest that the seasonal Yarkovsky effect could potentially force sub-m meteoroids to high i values.

To verify the accuracy of these results, we calculated the seasonal Yarkovsky accelerations for three representative bodies (i.e., $R = 1$, 10, and 100 m) at each integration time step ($\Delta t = 30$ days) and then calculated the net Δa and Δi changes over 1 Myr using Gauss's perturbation equations (Burns 1976),

$$\frac{da}{dt} = \frac{2a^{3/2}}{(\mu(1-e^2))^{1/2}}[R_p e \sin f + T_p(1 + e \cos f)] \quad (38)$$

and

$$\frac{di}{dt} = \frac{r N_p \cos(\nu + f)}{H}. \quad (39)$$

Here, $\mu = GM_\odot$, r is the distance from the Sun, f is the true anomaly, ν is the argument of pericenter, H is the angular momentum, and R_p, T_p, N_p are components of the instantaneous perturbing force on the body in the radial, transverse, and normal directions. Substituting in the relevant values and integrating, we found no significant changes between these results and those
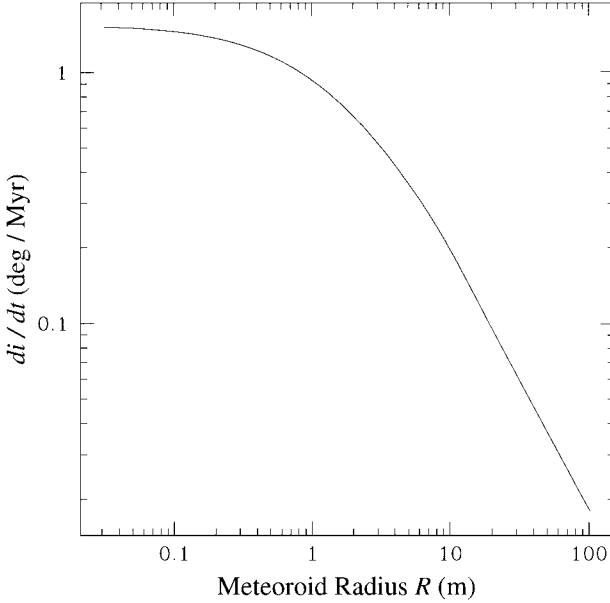
FIG. 6. Seasonal mean di/dt changes, averaged over one revolution, for various meteoroid sizes when $\hat{b} = (0.707, 0.0, 0.707)$. The test meteoroids have the same starting conditions and material properties as the objects described in Fig. 4. No planetary perturbations are included. Note that di/dt values increase as R decreases, in contrast to the da/dt results which are similar in shape to the seasonal da/dt results seen in Fig. 4. These high di/dt values are sharply curtailed once planetary perturbations are included.

values can add on one another, leading to large di/dt changes (Eq. (39)).

The $R = 10$ m case shows a much larger lag angle than the $R = 1$ m case, so the maximum in-plane acceleration vector has a substantial transverse component. This can lead to significant da/dt changes provided the acceleration magnitude is large. For our chosen thermal parameters, a $R = 10$ m body provides just the right mix of lag angle and thermal acceleration to maximize da/dt. The larger lag angle also decreases the magnitude of di/dt to some degree, though the more important effect is the factor of 5 decrease in acceleration magnitude over the $R = 1$ m case. This explains the di/dt drop-off for larger bodies seen in Fig. 6.

The $R = 100$ m case shows a larger lag angle than before, though it is coupled with significant decrease in thermal acceleration. The combination leads to even smaller though nonnegligible da/dt and di/dt rates. Figure 5 shows that an eventual

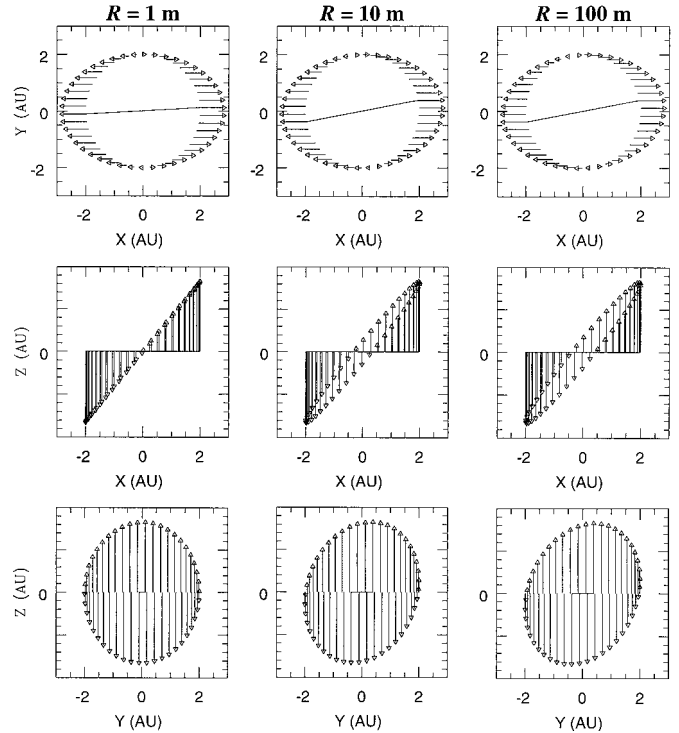found by our YS code. Thus, we have some confidence that the YS code is yielding correct values.

To gain intuition about the da/dt and di/dt vs R trends, we plotted the seasonal Yarkovsky acceleration components (x, y, z) over selected time steps for $R = 1, 10,$ and 100 m bodies making a single revolution around the Sun (Fig. 7). Recall that the seasonal force always points along the spin axis direction $(\hat{b})$. The acceleration vectors have been scaled by an arbitrary factor so they are easier to see. We have also drawn a line between the maximum acceleration vectors on each plot to give a sense of the thermal lag angle associated with the seasonal effect. If there were no thermal lag, the acceleration vectors in the xy plots would be mirror images of one another across the $x = 0$ line, such that a horizontal line would extend between the maximum vectors pointing in the $+x$ and $-x$ directions. The xz plot would also have a point instead of a line.

Examining the $R = 1$ m case, we find that the lag angle shown in the xy plot is small even though the acceleration vectors are large. Small lag angles imply that the largest seasonal "kicks" in the orbital plane are applied in a direction nearly radial to the Sun, while the smallest kicks are applied in the nearly transverse direction. It is clear from the perturbation equations (Eq. (38)) that this can only lead to minor changes in a. The situation is reversed for the out-of-plane forces (xz and yz plots), however, with the largest "kicks" coming when $\cos(\nu + f)$ is near ± 1. Since the acceleration vectors conveniently change signs on either side of the Sun, and r and H are essentially constant, N_p

FIG. 7. Seasonal Yarkovsky acceleration vector components (x, y, z) over selected time steps for $R = 1, 10,$ and 100 m bodies making a single revolution around the Sun. Starting conditions, spin axis orientation, and material properties are the same as in Fig. 6. The acceleration vectors have been scaled by arbitrary factors for each meteoroid size to make them visible; the $R = 1$ m test case has a maximum acceleration vector nearly 5 times as long as the maximum vector on the $R = 10$ m test case, and nearly 50 times as long as the maximum vector on the $R = 100$ m test case. A line has been drawn between the maximum acceleration vectors on each plot to make the thermal lag angle easier to see. Here, $R = 1$ m has the smallest lag angle but the largest acceleration vectors, yielding small da/dt and large di/dt rates; $R = 100$ m has a large lag angle but tiny acceleration vectors, yielding small (but considerable for its size) da/dt and small di/dt rates; $R = 10$ m strikes a balance between these two cases, yielding high da/dt and moderate di/dt rates.

equilibrium is reached at larger R between these two factors, such that the body is no longer so dependent on its distance from the Sun. (See the end of Section 4.1 for more explanation.)

To summarize, these plots verify that the seasonal Yarkovsky effect can produce large inclination changes in small meteoroids when their spin axis is out of the orbital plane. The question of what happens to da/dt and di/dt when planetary perturbations are included will be addressed in the next section.

4.3. Effects of Secular Perturbations on the Yarkovsky Effect

So far, we have only investigated the relatively simple case of how the Yarkovsky effect modifies the orbital motion of meteoroids around the Sun when no other perturbing forces are present. In this section, we treat the more realistic case of meteoroids evolving in a system where their motions are perturbed by the gravitational forces of planets Venus through Neptune. Issues that now become important (and more difficult to treat analytically) are: (i) precession (regression) of a meteoroid's apsides (nodes), (ii) secular perturbations inducing a forced eccentricity and inclination component into a meteoroid's osculating e, i values, and (iii) mean-motion and secular resonance phenomena, which can produce rapid and chaotic changes in a meteoroid's osculating e, i values. In addition, we must also become concerned with the long-term behavior of the meteoroid's spin axis, which can precess under the influence of solar torques. As spin axes and orbital motions slowly evolve, the magnitude and direction of the Yarkovsky thermal forces must change as well. The important effect of meteoroid collisions will be discussed in Section 4.4.

4.3.1. Spin axis and orbit normal precession rates.
The long-term behavior of the spin axis depends to a large degree on whether its precession rate is slower or faster than that of the orbit's plane. Ward (1992) discusses two limiting cases of interest, (a) if the normal to the meteoroid's orbital plane precesses much faster than the motion of the spin axis, then the latter precesses around the mean direction of the orbital normal, which is normal to the invariable plane, and (b) if the motion of the spin axis is much faster than the motion of the orbit normal, then the spin axis can maintain a nearly constant obliquity as it precesses around the orbit normal. To determine which case is applicable for meteoroids, we need to first find the spin axis precession time scale and the precession time scale of the orbital node.

The spin axis precession time scale induced by solar torques on an axially symmetric object orbiting the Sun has been estimated by Burns and Tedesco (1979) to be

$$\tau_{\text{spin}} = \frac{T^2}{P \Delta}, \qquad (40)$$

where T is the orbital period, P is the spin period, and $\Delta = (C - A)/C$, the relative difference in the meteoroid's moments of inertia C and A. If we apply some reasonable parameters for an $R = 1$ m body (e.g., $\Delta \sim 0.1$, $P = 0.01$ h, and $a = 2$ AU), we find that $\tau_{\text{spin}} = 70$ Myr. Assuming that most objects have spin

periods which scale with R (as described above), we conclude that $\tau_{\text{spin}} \gtrsim 0.1$ Myr for sub-km objects.

The nodal precession rate in the main belt is 26 in yr^{-1} at 2 AU (A. Morbidelli 1998, personal communication), which corresponds to a precession time scale of $\tau_{\text{node}} \sim 0.05$ Myr. Since $\tau_{\text{spin}} \gg \tau_{\text{node}}$ for meteoroids, we can assume that the spin axis precesses around the normal to the invariant plane. In fact, for $R < 10$ m, it is reasonable to assume in the code that meteoroids have fixed $\hat{b}$ orientations relative to inertial space. Section 4.3.2 and Vokrouhlický and Farinella (1998a) also treat this problem.

Note that an updated version of Eq. (40) includes a factor of $2/(3 \cos \xi)$, where ξ is the meteoroid's obliquity (D. Vokrouhlický 2000, personal communication). While the 2/3 factor reduces the forced precession period, the $1/\cos \xi$ term, on average, increases it significantly, which strengthens the conclusion that $\tau_{\text{spin}} \gg \tau_{\text{node}}$. The updated equation is sometimes called the Hipparcos precession formula.

4.3.2. Estimated change in orbital elements from the perturbation equations.
An estimate of how a meteoroid's a and i values change with time under the influence of the Yarkovsky effect and secular planetary perturbations can be gained by substituting the Yarkovsky accelerations (diurnal and seasonal) into the perturbation equations. Since the algebra is long and tedious, we only describe the procedure and results here. Interested readers can find additional detail in Rubincam (1995).

We first need to find the radial, transverse, and normal directions of the Yarkovsky accelerations. The rotation matrix to make this time-dependent transformation can be constructed from the set of Euler angles

$$M = [\theta]_z [i]_x [\Omega]_z, \qquad (41)$$

where the third, second, and first rotation angles (in brackets) are rotated about the third, second, and first rotation axes (in subscripts) (i.e., for $[\theta]_z$, you rotate about the z axis by an amount θ); θ is the angle in the plane of the orbit between the ascending node and the radius vector to the meteoroid, and Ω is the longitude of the ascending node. Multiplying the seasonal accelerations by M and substituting the radial and transverse expressions, we get a complex expression for da/dt which can be simplified by assuming that the meteoroid is on a circular orbit and the apsides and nodes circulate uniformly, a reasonable assumption for meteoroids acting under the influence of secular planetary perturbations. Averaging over an orbital period allows us to drop the fast periodic terms, leading to a seasonal rate of change for the semimajor axis of

$$\frac{da}{dt} = -\frac{1}{n} \left[C_{\text{sea}} F_{\oplus} \left(\frac{1 \text{ AU}}{a} \right)^2 \sin \varepsilon_{\text{sea}} \right] (1 - b_z^2), \qquad (42)$$

where b_z is the component of the unit spin vector normal to the invariable plane (Rubincam 1998). The maximum magnitude of $|da/dt|$ for the diurnal effect can be found using same expression, as long as we replace C_{sea} with C_{diur}, $\sin \varepsilon_{\text{sea}}$ with $\sin \varepsilon_{\text{diur}}$, and drop the quantity $(1 - b_z^2)$.

Inserting values into this expression, we can readily duplicate the maximum seasonal and diurnal results shown in Fig. 3. Thus, secular planetary perturbations do not change the Yarkovsky da/dt rate in any significant way.

We can solve for the seasonal rate of change in inclination in the same manner, yielding

$$\frac{di}{dt} = \frac{C_{\text{sea}}F_{\oplus}}{8na}\left(\frac{1\,\text{AU}}{a}\right)^2 \sin 2i \sin \varepsilon_{\text{sea}}\left(1 - 3b_z^2\right). \quad (43)$$

Note that this equation replaces Eq. (31) in Rubicam (1995), which should have a $\sin 2i$ term instead of a $\cos i$ term.

From inspection, we see that $i = 0°$ orbits yield $di/dt = 0$ values, regardless of the choice of b_z. This contradicts our previous results which showed large inclination changes for spin axes oriented at a $45°$ angle to the orbital plane. The explanation is that orbital precession allows the seasonal acceleration to increase i at a particular nodal value and decrease it again $180°$ later, yielding periodic terms but a secular zero. Since we force $\hat{b}$ to keep a constant obliquity relative to the inertial z axis, the seasonal force terms cancel out over a revolution. If i is nonzero, however, the meteoroid's obliquity varies as the node swings around. Since the seasonal force depends on obliquity, we do not get a complete cancellation $180°$ later, leaving a secular rate. Still, the resultant rate is much diminished over the no-precession case described previously.

The maximum secular di/dt rate occurs when $i = 45°$ and $b_z^2 = 1$. With the thermal parameters described in Section 4.1, the maximum di/dt rates for $R = 1$, 10, and 100 m bodies at $a = 2$ AU are $0.007°$, $0.03°$, and $0.004°$ Myr^{-1}, much reduced from those presented in Table I. Frequent collisions capable of modifying the orientation of $\hat{b}$ would reduce these rates even more. Rubicam (1995) approximated this effect by assuming all $\hat{b}$ orientations were possible over a meteoroid's lifetime (i.e., $\langle b_z^2 \rangle = 1/3$). Substituting this value into Eq. (43), we find that di/dt changes go to zero. Thus, we conclude that seasonal Yarkovsky effect produces small-to-insignificant i changes over the lifetimes of most meteoroids, provided their nodes circulate uniformly.

4.3.3. Changes in orbital elements from direct integration. Checking seasonal and diurnal da/dt, de/dt, and di/dt rates using the YS code is nontrivial, since the inclusion of planets like Jupiter and Saturn introduces effects (e.g., chaotic resonances, forced e and i terms) that can be orders of magnitude more efficient at changing osculating es and is than the Yarkovsky effect. For example, our test meteoroid from before ($a = 2$ AU; $e = 0.0$, $i = 0°$) lies near the ν_6 and ν_{16} secular resonances and the 4:1 mean-motion resonance with Jupiter; together they are powerful enough to pump up a meteoroid's e and i to large values in less than 1 Myr. As e and i change, so must the magnitude of the Yarkovsky accelerations and the orientation of the orbit plane. These "feedback loops" can be difficult to model except through numerical integration, making drift rates ultimately difficult to predict.

To demonstrate this, we integrated variously sized meteoroids on ($a = 2$ AU; $e = 0.0$, $i = 0°$) orbits using the YS code. Our goal was to look for secular trends in da/dt. We integrated for 1,000 years and 10,000 years and included the planets Venus–Neptune. We hoped that the short integration times would help minimize the effects of resonant pumping of e and i, and $\hat{b}$ was placed in the orbit plane ($\hat{b} = 1.0, 0.0, 0.0$) to get the maximum seasonal drift rate.

To obtain a control, we turned off the Yarkovsky effect and integrated a test body in the YS code for our selected time. We found that planetary perturbations alone were enough to introduce significant changes in the osculating orbit, ($a = 2.000033$ AU, $e = 0.00324$, $i = 0.17574°$) after 1,000 years of integration, and ($a = 1.999720$ AU, $e = 0.03141$, $i = 1.58542°$) after 10,000 years of integration. Next, we integrated our suite of meteoroids for the same integration times (with the Yarkovsky effect on) and subtracted our control a (with the Yarkovsky effect off) from the new a values. Our results are shown in Fig. 8. Results from Fig. 4 (i.e., no planetary perturbations included in the integration) have been included as a second control.

We see that after 1,000 years, our da/dt results are lower by roughly a factor of 1.4 vs the "no-planets" control. A comparison after 10,000 years, however, is dramatically different; bodies near $R = 10$ m now have a faster da/dt rate than the "no-planets" control, while objects near $R = 2$ and 30 m have much slower rates than the "no-planets" control. This variance is caused, in part, by the meteoroid's nodal precession rate ($d\Omega/dt$), which
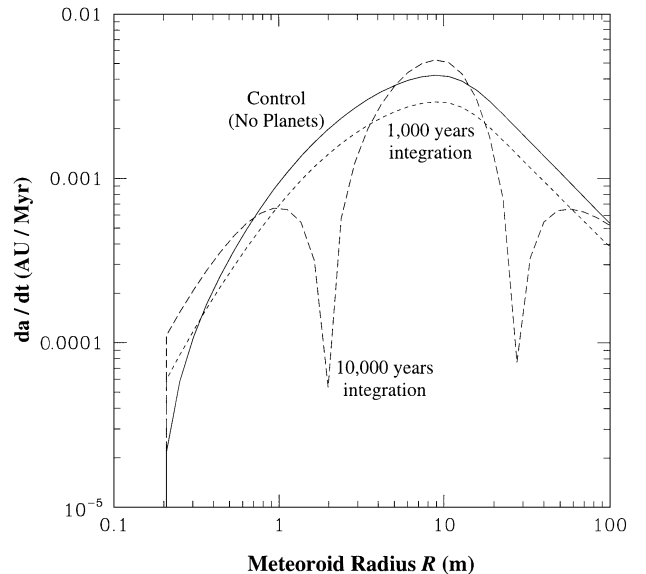
FIG. 8. Dynamical evolution of test meteoroids under the seasonal Yarkovsky effect. Orbital and material properties are the same as in Fig. 4. Here, $\hat{b} = (1.0, 0.0, 0.0)$ (i.e., in the orbit plane). The control was integrated without planetary perturbations included. For the other test cases, planets Venus–Neptune were included. Integration time scales lasted 1,000 and 10,000 years. The variance between the curves is caused, in part, by the nodal precession rate of the meteoroids ($d\Omega/dt$), which is influenced by both planetary perturbations and the Yarkovsky accelerations.

is influenced by both planetary perturbations and the Yarkovsky accelerations. Since resonance phenomena generate a small inclination in each meteoroid's orbit, the seasonal "kick" along its spin axis (i.e., $\hat{x}$ direction in inertial space) is no longer entirely in the orbit plane. From the perturbation equations, we know that normal forces cause Ω to precess, changing the orientation of the orbit plane and thus the direction of the orbital "kick" relative to that plane. Depending on the precession rate, these forces undergo constructive or destructive interference, in turn increasing or decreasing a relative to the control.

The same method cannot be used to estimate de/dt rates, since small changes in orbital energy modify the object's "depth" in the resonance and the degree of e pumping. For example, the maximum de/dt rates, found for $R \sim 10$ m after 1,000 and 10,000 years of integration time, are -6.8×10^{-4} and -0.025 Myr^{-1} (!), respectively. The latter result is far too high because no appropriate control value could be used.

Similarly, di/dt rates are difficult to calculate, though experience suggests that secular resonances like the ν_6 are not nearly as effective at pumping up i values as at pumping up e values. Our results match these expectations; the maximum di/dt rates, found for $R \sim 10$ m after 1,000 and 10,000 years of integration time, are $0.002°$ and $0.008°$ Myr^{-1}, respectively. Based on these low di/dt values, which may be enhanced by planetary perturbations, we conclude that significant secular i changes in our long-term meteoroid evolution results are unlikely.

Our final test was to examine the long-term integration results of $R = 1$ m meteoroids started in a number of positions in the inner main belt. As expected, no evidence was found for important e and i trends unless a resonance was involved. These results will be discussed in much greater detail in Section 5.

To summarize, we conclude that da/dt predictions using the perturbation equations do yield insights into the behavior of dynamically evolving meteoroids over long time scales, particularly when these meteoroids are far from mean-motion or secular resonances. The only way to get accurate drift rates in the vicinity of resonances, however, is through direct numerical integration. Meteoroid de/dt and di/dt rates caused by Yarkovsky thermal forces tend to be small when planetary perturbations are present. Precession rates of Ω are needed to determine the magnitude of da/dt, de/dt, and di/dt.

4.4. Effect of Collisions on Meteoroids

Meteoroids residing in the inner Solar System frequently undergo collisions with other small bodies. These events can damage or destroy the meteoroid, and they also transmit angular momentum to the meteoroid. As a result, the meteoroid's spin axis is reoriented, potentially altering the sign of the diurnal drift rate and the magnitude of both the seasonal and the diurnal drag rates. For this reason, we have included collisions in our YS code.

Using the method described in Farinella et al. (1998a), we assume the mean interval between spin axis reorientation events

for a target of radius R can be expressed as

$$\tau_{\text{rot}} = \frac{1}{P_i R^2 N(r_{\text{rot}})} \tag{44}$$

with P_i the intrinsic collision probability of the target body with other main belt asteroids (Bottke et al. 1994a), r_{rot} the projectile size needed to "flip" the meteoroid's spin axis, and $N(r_{\text{rot}})$ the cumulative number of main belt asteroids with $R > r_{\text{rot}}$. Farinella et al. estimated r_{rot} to be

$$r_{\text{rot}} = \left(\frac{2^{3/2} \rho_t \omega R}{5 \rho_p V} \right)^{1/3} R \tag{45}$$

with ρ_t and ω the target's density and spin rate, ρ_p the projectile's density, and V the impact velocity. The P_i and V values, which depend on the target's a, e, i location, were mapped in Bottke et al. (1996); we have slightly updated the map for the YS code.

The cumulative size-frequency distribution of small main belt asteroids needed to find $N(r_{\text{rot}})$ was estimated by Farinella et al. (1998a) to be

$$N(r) = 3.5 \times 10^5 \left(\frac{r}{1 \text{ km}} \right)^{-5/2}. \tag{46}$$

Note that there is considerable uncertainty in this estimate. Observational evidence suggests that the main-belt size distribution for asteroids smaller than a few km in diameter may have a more shallow slope than that used in Eq. (46) (Jedicke and Metcalfe 1998). If so, collisions will be less frequent than predicted.

The YS code uses a random deviate to determine whether a spin reorientation event has taken place. Checks are made every 10,000 years of computation time, and τ_{rot} is assumed to be a "half-life" parameter. When a critical collision occurs, the YS code assigns a new random orientation for the test body before continuing the integration.

A similar procedure is also available in the YS code to treat catastrophic disruption events. However, since testing large numbers of particles for tens of Myr is computationally expensive (e.g., Vokrouhlický and Farinella 2000), we have turned off the disruption function for this paper. These events are still recorded, though, so we can easily include them afterward using post-processing. As we gain more intuition on how small bodies evolve in the main belt, our simulations grow in complexity to account for these effects.

5. RESULTS

With the YS code tested, we are now ready to apply it to meteoroid-delivery issues. Our use of the code in this paper, however, is constrained by computational expediency; we choose to examine specific dynamical issues which are difficult to explore using analytical methods (i.e., effects of chaotic resonances; planetary close encounters). Our goal is to characterize the orbital evolution of meteoroids well enough to apply these results

to fast Monte Carlo codes, which may be better suited to investigate the evolution of numerous bodies with varying size-frequency distributions, thermal properties, and spin rates.

To accommodate the small number of particles used in our runs, we have traded some realism for diagnostic purposes. For example, meteoroids ejected from their parent asteroids have trajectories and velocities that are not well constrained or understood. Rather than try to study all parts of this vast parameter space with a limited number of bodies, we instead start our meteoroids at the parent asteroid in the same orbit. This way, we can follow what happens to the meteoroids without worrying about how launch conditions have biased the result. It is important to keep in mind, however, that ejection events can and probably do throw meteoroids to the vicinity of chaotic resonances, shortening their travel time considerably . We have also eliminated meteoroid disruption events, since they diminish our limited statistics. We justify this by noting that the typical integration time used in this paper (50 Myr) is comparable to the CRE ages of some stony meteorites (Marti and Graf 1992).

The proper semimajor axes and inclinations (i.e., effects of planetary perturbations have been removed) of the parent bodies tested in Section 5 are plotted in Fig. 9. Starting osculating orbital elements and outcome statistics for the same bodies are displayed in Table II.

5.1. Meteoroids from 6 Hebe

We start our investigation by tracking the delivery of meteoroids from the asteroid 6 Hebe, a 200 km diameter S-type asteroid with osculating orbital elements $a = 2.425$ AU, $e = 0.169$, and $i = 15.05°$. Precise orbital elements for this body (and the other parent bodies discussed in this paper) were found using the Horizons On-Line Ephemeris (Chamberlin $et\ al$. 1997). Hebe's high inclination places it near the $3 : 1$ and ν_6 resonances; we expect these "escape hatches" to be the main routes taken by Hebe meteoroids on their way to EC orbits. Hebe also happens to be one of the largest asteroids located near both resonances, making it a big target for impactors. Since an asteroid's colli-
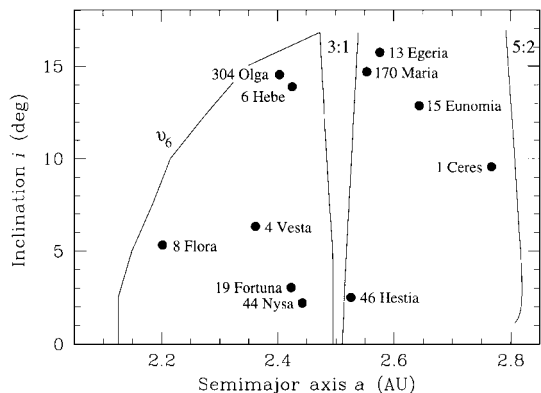

FIG. 9. Proper a and i values for the parent bodies examined in Section 5. The approximate positions of the $3 : 1$, $5 : 2$, and ν_6 resonances are also shown. Note that proper orbital elements are slightly different than the starting conditions shown in Table II, which use osculating orbital elements.

sion rate is a function of its geometrical cross section, Hebe may produce a far greater share of fragments than smaller individual parent bodies at comparable locations. If true, it is plausible to assume that a substantial fraction of all S-type asteroid meteorites are from Hebe (e.g., Farinella $et\ al$. 1993). Support for this hypothesis comes from conspicuous similarities between Hebe's spectral signature and the composition of H-type ordinary chondrites (Gaffey and Gilbert 1998). Several reports have even suggested that Hebe is the primary source of the ordinary chondrites meteorites (Migliorini $et\ al$. 1997a).

For our YS runs, we tracked two sets of stony meteoroids on Hebe-like orbits, varying only the thermal conductivity K parameter, which influences the drift rate. Each set contained 50 $R = 1$ m bodies, and each of these bodies was started with a random spin axis orientation $\hat{b}$. The meteoroid swarms were tracked for 50 Myr of integration time. Venus–Neptune were included in the integrations. Orbital parameters were output every 10,000 years. The integration time step was 30 days, reasonable for perihelion distances (q) larger than 1 AU. We caution, however, that a few close encounters with Mars may be missed

TABLE II
Summary of Meteoroid Evolution Outcomes

Parent	a (AU)	e	i (deg)	1st MC (Myr)	1st EC (Myr)	$\langle T_{MC} \rangle$ (Myr)	$\langle T_{EC} \rangle$ (Myr)	% MC	% EC
1 Ceres	2.770	0.077	10.58	6.81	6.82	23.0 ± 11.2	24.5 ± 11.6	44	34
4 Vesta	2.361	0.090	7.14	14.34	15.35	29.6 ± 10.1	31.7 ± 9.0	42	36
6 Hebe	2.425	0.202	14.77	5.53	10.88	15.4 ± 10.2	27.0 ± 12.1	88	68
8 Flora	2.202	0.156	5.89	1.36	6.82	8.1 ± 11.4	17.8 ± 10.4	94	54
13 Egeria	2.575	0.087	16.53	5.68	6.23	19.0 ± 10.2	22.9 ± 11.8	74	70
15 Eunomia	2.643	0.187	11.76	12.97	14.56	31.0 ± 9.6	31.4 ± 9.2	54	42
19 Fortuna	2.443	0.159	1.57	4.57	4.69	23.0 ± 12.2	22.1 ± 13.2	48	26
44 Nysa	2.423	0.150	3.70	9.79	10.33	32.6 ± 13.3	25.3 ± 13.4	26	14
46 Hestia	2.524	0.173	2.34	1.14	1.15	9.9 ± 12.0	12.0 ± 13.3	70	64
170 Maria	2.554	0.064	14.42	4.57	4.81	15.8 ± 12.0	19.0 ± 13.5	64	64
304 Olga	2.404	0.220	15.82	1.31	4.49	11.0 ± 10.4	17.8 ± 10.9	98	92

when/if the bodies reach Mars-crossing (hereafter MC) orbits. For this reason, future dynamical evolution studies in the MC regime should use smaller time steps. To avoid anomalous results with this time step, bodies with $q < 1.0$ AU were removed from the run. Thermal and material properties were chosen to be consistent with S class asteroids: $C_p = 680$ J kg^{-1} K^{-1}, $\epsilon = 0.9$ (Lebofsky and Spencer 1989), and $A = 0.08$ (Helfenstein *et al.* 1996). Other relevant parameters include bulk density ($\rho = 3500$ kg m^{-3}) and spin period ($P = 0.01$ h).

5.1.1. Hebe meteoroids: Slow drift rate. A basaltic-like thermal conductivity was chosen for the first set of meteoroids ($K = 2.65$ W m^{-1} K^{-1}). This value produces maximum seasonal and diurnal da/dt rates of $\sim -5 \times 10^{-4}$ and $\sim \pm 4 \times 10^{-4}$ AU Myr^{-1}, respectively (found with planetary perturbations off). We estimate the distances between 6 Hebe and the 3 : 1, ν_6 resonances to be $\Delta a \sim 0.057$ AU, -0.084 AU, respectively (Morbidelli and Gladman 1998). For reference, well-aimed and well-timed meteoroids ejected from Hebe would need v_∞ velocities (the velocity after escape has occurred) in excess of ~ 200 m s^{-1} to reach either resonance. Since meteoroids moving at the maximum da/dt rates listed above would still take over 100 Myr to reach the either resonance (much longer than our 50 Myr integration time or the assumed collisional disruption time scale), we use this run to gauge general particle behavior in the YS code.

Our results show that the maximum distance traversed by any single meteoroid in this run over 50 Myr is -0.037 AU (from 2.425 to 2.388 AU), while the mean distance traversed by all 50 bodies is -0.019 ± 0.01 AU. The substantial spread in distance is caused by positive drift rates generated by the diurnal effect. Similarly, the mean drift rate $\langle da/dt \rangle$ is $\sim (-3.8 \pm 2.0) \times 10^{-4}$ AU Myr^{-1}, not very different from the maximum values described above. The mean number of $\hat{b}$ reorientation events in the particle swarm was 11.5 ± 4.0; one body saw only 4 $\hat{b}$ "flips" while another saw 21.

Secular planetary perturbations produced periodic changes in the eccentricities and inclinations of the bodies, making it difficult to distill out secular trends. In general, e for the 50 bodies varied between ~ 0.04 and ~ 0.28. Minor e oscillations, with an amplitude of ~ 0.02 and a period of $\sim 50,000$ years, ride on larger e oscillations with an amplitude of 0.11 and a period of ~ 0.4 Myr. The amplitude of the large-scale e oscillations appears to grow as the meteoroids move inward. Oscillations in i do not appear to have a discernible pattern with 10,000-year time steps, though the period appears to be roughly 30,000–40,000 years with an amplitude near 3°. The min/max values are 11.5° and 17.7°, respectively. No secular trends are observed.

5.1.2. Hebe meteoroids: Fast drift rate. For our second run, we chose $K = 0.0015$ W m^{-1} K^{-1}, appropriate if our meteoroids are porous or if they have a fine dusty surface (Rubincam 1998, Farinella *et al.* 1998a). The maximum seasonal and diurnal da/dt rates for this K value (no planetary perturbations included) are $\sim -1 \times 10^{-3}$ and $\sim \pm 2 \times 10^{-2}$ AU Myr^{-1}, much

higher than those for $K = 2.65$ W m^{-1} K^{-1}. With these drift rates, meteoroids should reach the ν_6 resonance well within 50 Myr. Note that a recent improved treatment of the seasonal effect for regolith-covered asteroids (Vokrouhlický and Brož 1999) suggests that seasonal mobility may be reduced by as much as a factor of 10 than our estimated value. In this regime, however, the diurnal drift rate dominates to such a degree that our results remain accurate.

Since the maximum diurnal drift rate is much larger than the maximum seasonal drift rate, particles will move both inward and outward in a, depending on spin direction. Collisions, however, produce multiple $\hat{b}$ changes, causing diurnal da/dt to frequently change sign and magnitude. This diurnal random walk allows the seasonal effect to push $\langle a \rangle$ inward with time. For example, after 9 Myr of integration (i.e., just before some particles begin to enter the ν_6 resonance), $\langle a \rangle = 2.401 \pm 0.03$ AU, a $\langle da/dt \rangle$ drift rate of $(-2.7 \pm 3.4) \times 10^{-3}$ AU Myr^{-1}.

Figure 10 shows the orbital elements of a representative meteoroid evolving under the combined influence of the seasonal and diurnal Yarkovsky effects, collisions, distant perturbations, and planetary close encounters. The open circles show the nine spin axis reorientation events produced over 42.32 Myr. The starting b_z value is -0.790, causing the object to initially evolve inward
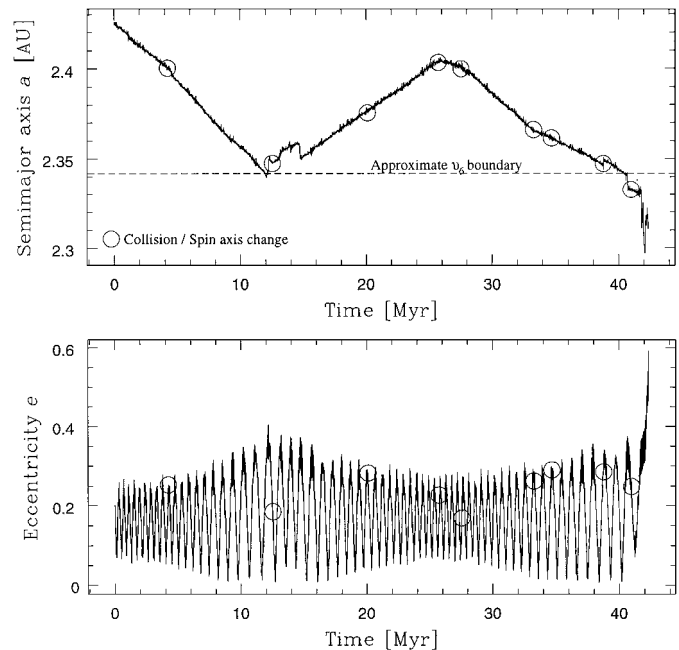

FIG. 10. Dynamical evolution of an $R = 1$ m Hebe-like meteoroid. Seasonal and diurnal forces are included, as are perturbations from planets Venus–Neptune. The orbit starts at $a = 2.425$ AU, $e = 0.169$, and $i = 15.05°$, with $\hat{b} = (0.581, 0.196, -0.790)$. Thermal and material properties were chosen to be consistent with S-class asteroids: $C_p = 680$ J kg^{-1} K^{-1}, $\epsilon = 0.9$, $A = 0.08$, $\rho = 3500$ kg m^{-3}, and $P = 0.01$ h. Thermal conductivity was set low enough ($K = 0.0015$ W m^{-1} K^{-1}) to allow a fast da/dt drift rate. The open circles show the nine collision/spin axis reorientation events produced over 42.32 Myr. Large jumps in a are caused by encounters with the $(m_J, n_S, k) = (9, -6, -2)$ mean-motion resonance between Jupiter–Saturn–asteroid, located near $a = 2.35$ AU.

under the predominant influence of the diurnal Yarkovsky effect. The first spin axis change modifies b_x and b_y, but leaves b_z strongly negative, allowing the evolution to continue inward. As the object draws closer to the ν_6 resonance, distant perturbations grow in strength, increasing the amplitude of the forced e component. Then, at 12.20 Myr, the meteoroid encounters a three-body mean-motion resonance (Jupiter, Saturn, meteoroid) (Migliorini *et al.* 1998, Murray *et al.* 1998, Nesvorný and Morbidelli 1998, Morbidelli and Nesvorný 1999). Note the regular but steady increase in amplitude seen among osculating e at this position, the increase in a, and the comparable behavior for similar a values at ∼40 Myr. (The increase in the oscillation period of e is probably related to the meteoroid's proximity to the ν_6 resonance.) Three-body resonances correspond to the equality $m_J \dot\lambda_J + n_S \dot\lambda_S + k\dot\lambda = 0$, where $\dot\lambda_J$, $\dot\lambda_S$, $\dot\lambda$ are the mean-motions of Jupiter, Saturn, and the asteroid, and m_J, n_S, k are integers. This particular resonance, the $(m_J, n_S, k) = (9, -6, -2)$, splits into three resonances between 2.34 and 2.36 AU (Morbidelli and Nesvorný 1999). Each one influences the evolution of this particular meteoroid over its lifetime. A discussion of how drifting meteoroids and mean-motion resonances interact (and change the subsequent dynamical evolution of meteoroids) can be found in Section 5.1.3.

Resonance encounters, however, do not change $\hat{b}$, such that the meteoroid's inward drift continues at the same rate for another 0.33 Myr after the resonance encounter. Then, at 12.53 Myr, another spin-axis reorientation event occurs, giving b_z a positive value (0.868). This causes the meteoroid to reverse direction and slowly spiral outward under the diurnal Yarkovsky effect. Enduring a few more resonance encounters (and a kicks), the body evolves away from the ν_6 resonance, reducing the forced e amplitude all the way back to its starting value. Finally, at 25.74 Myr, another collision gets the meteoroid moving inward again. Several more spin axis flips occur, but they result in b_z values which are either strongly negative (diurnal drag dominates) or near zero (seasonal drag dominates). Eventually, after resonance encounters near ∼40 Myr, the object drifts deeply into the ν_6 resonance, causing e values to get pumped up to an EC value. At this point, the code records the exit data and ends the run.

We can use Fig. 10 to make some observations. First of all, the ν_6 resonance does not appear to have a sharp boundary; particles spiraling inward see their forced e amplitudes increase to MC values (e.g., near perihelion $q \sim 1.66$ AU) well before they cross the nominal ν_6 boundary estimated numerically by Morbidelli and Gladman (1998). This behavior was first discovered by Wetherill and Williams (1979) during their search for the sources of differentiated meteorites. Second, meteoroids often encounter weak resonances well before they enter the ν_6 resonance; these effects can delay the inward evolution of the meteoroid by a few Myr. Third, we find that the large e jumps commonly associated with the ν_6 resonance (e.g., Morbidelli *et al.* 1994) only occur when our test bodies are deep inside the resonance; objects near the periphery may have their evolution
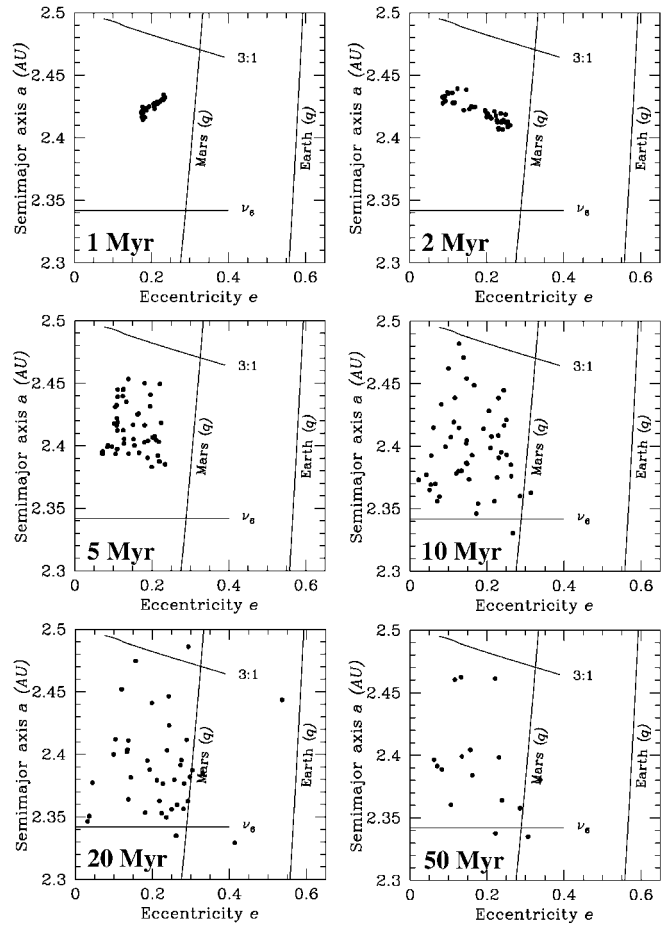
FIG. 11. Snapshots from the orbital evolution of 50 Hebe-like meteoroids. Starting orbit, integration parameters, meteoroid sizes, and material properties are the same as in Fig. 9. Approximate positions of the 3 : 1 and ν_6 resonances and perihelion values (q) needed to reach Mars- and Earth-crossing orbits are shown. Meteoroids reaching Earth-crossing orbits are removed from the run. The meteoroid swarm is shown after 1, 2, 5, 10, 20, and 50 Myr of integration. The dynamical range of osculating e increases as the objects approach the ν_6 resonance. Most meteoroids reach Mars-crossing orbits well before entering the ν_6 resonance.

modified by libration amplitude increases or weak resonant behavior. Finally, the amplitude of the forced i oscillations (not shown) do not appear to significantly change until the object is well inside the ν_6 resonance (i.e., outside the resonance, i stays between 12° and 16.5°).

Snapshots of the orbital evolution of our Hebe-like meteoroid distribution are shown in Fig. 11. Solid lines show the approximate values needed to reach MC orbits, EC orbits, the 3 : 1 resonance, and the ν_6 resonance, the latter assuming the meteoroids have a mean i between ∼14° and 15°. The first two frames show the meteoroids after 1 and 2 Myr of evolution. Note how the Yarkovsky effect causes the bodies to spread inward and outward in a, while secular planetary perturbations cause oscillations in osculating e. After 5 Myr of evolution, the bodies cover a large section of the inner main belt. After 10 Myr, one

object has entered the ν_6 resonance. Despite this, at this time in the integration, 15 bodies (30%) have achieved MC orbits (e.g., note the object seen beyond the MC orbit boundary in the figure). After 20 Myr of evolution, objects can be seen in the 3:1 resonance, the ν_6 resonance, and on MC orbits. Nine particles have reached EC orbits and have been removed from the run. The last frame shows the meteoroid distribution at the end of the integration (50 Myr). Only 16 particles remain, with two more working their way deeper into the ν_6 resonance.

In terms of overall statistics, we found that 44 (88%) of the meteoroids reached MC orbits over 50 Myr, while 34 (68%) reached EC orbits. The shortest intervals needed for particles to reach crossing orbits with Mars and Earth were 5.53 and 10.88 Myr, respectively. The median planet-crossing times for meteoroids with Mars and Earth were 11.92 and 23.33 Myr, respectively. Note that most particles become MC before well before they cross the derived "boundary" for the ν_6 resonance, implying the boundary itself can be difficult to measure. A related trend, though not apparent from Fig. 11, is that the meteoroids' forced e amplitude grows as the distribution nears the ν_6 resonance. This gives the overall distribution a roughly triangular shape on the (a, e) plot, with the tapered end of the triangle near the 3:1 resonance and the base near the ν_6 resonance. The shape is related to the dense distribution of Mars and three-body resonances in the inner main belt, making orbital behavior there more chaotic (Migliorini *et al.* 1998, Morbidelli and Nesvorný 1999). Finally, some bodies appear to reach MC orbits well away from the 3:1 or ν_6 resonances. For inward-drifting bodies, this outcome is caused by an increase in libration amplitude near the ν_6 resonance (Wetherill and Williams 1979). For outward-evolving bodies, this outcome is caused by the $(m_J, n_S, k) = (4, -2, -1)$ three-body mean-motion resonance at $a = 2.397$ AU (Morbidelli and Nesvorný 1999).

To help interpret the meteoroid evolution tracks presented in this paper, we now present a more thorough discussion of how resonances and drift forces interact and influence the dynamical evolution of meteoroids.

5.1.3. Resonance capture and jumps at mean-motion resonances. As Fig. 10 demonstrates, meteoroids frequently encounter weak mean-motion resonances as their orbits evolve inward or outward. Such mean-motion resonances are seen to alter the dynamical evolution of drifting bodies in two ways, resonance trapping and resonance jumping. Both features have been known previously for (i) satellite gravitational resonances (dynamically similar to our situation), where the evolution usually occurs through tidal forces (Goldreich 1965, Greenberg 1973, Peale 1986, cf. Weidenschilling and Jackson 1993), (ii) planetary gravitational resonances (Hamilton 1994), and (iii) Lorentz resonances on electrically charged dust (Schaffer and Burns 1992, Hamilton 1994), where Poynting–Robertson drag or other nongravitational forces cause the evolution. Since resonance zones tend to be narrow, drags are often taken to be constant across them (cf. Hamilton 1994). If this assumption is valid,

the dynamical effects of crossing a resonance should be insensitive to the cause of the orbital drift. That is to say, resonant dynamics driven by Yarkovsky drag should be identical to those previously studied, with one major exception: the diurnal Yarkovsky effect allows particles to drift through resonances in either direction with, as we will describe below, different consequences. This section briefly reviews the orbital behavior of point masses as they drift through isolated resonances and its application to our numerical simulations. We caution, however, that no one has yet analytically explored resonant dynamics in regions where resonances overlap or near three-body resonances. It is not yet clear whether drift through these regions is equivalent to evolution through isolated two-body resonances. In particular, since orbits are known to be chaotic throughout much of the asteroid belt, due to overlapping resonances, it is likely that simple analytical models are, at best, suggestive.

Previous studies (Peale 1986, Malhotra 1991) of isolated mean-motion resonances have derived a pendulum-like Hamiltonian (or energy integral) to follow the dynamics near the resonance. As the orbit evolves, the Hamiltonian changes accordingly. In such a formulation the level curves of the Hamiltonian display either of two morphologies: (i) the resonant variable circulates (apsides or nodes cycle freely) or (ii) it librates (apsides or nodes oscillate around an equilibrium configuration). Depending upon the direction that the resonance is approached, circulation may or may not evolve into a stable libration (trapping is possible although not guaranteed or capture is not possible). For capture into isolated mean-motion resonances, the body must drift toward the planet creating the mean-motion resonance. Such a straightforward criterion for capture is not yet available for three-body resonances. If capture fails, the body will "jump" the resonance. Accordingly, for capture into jovian mean-motion resonances, da/dt must be outward, whereas, for capture into martian resonances, it must be inward.

Resonant capture takes place when orbital drift due to drag balances resonant perturbations (i.e., $[da/dt]_{\text{drift}} + [da/dt]_{\text{res}} = 0$), meaning that the orbital period remains commensurate with the forcing period. The trapping probability depends on the relative strengths of the drift force and resonance involved; strong drift forces or weak resonances make capture much less likely. Numerical integrations of trapping events using the YS code (where the Yarkovsky effect accounts for the drift) show that a stays more-or-less constant while e increases with time. Once some limiting value of e is attained, the meteoroid is released from the resonance. Note that failed trapping events will generally cause jumps (plus or minus) in e and/or i. Jumps occur at gravitational resonances when the meteoroid is moving away from the planet that is involved in the resonance or when it is moving toward the planet but with a drift rate that is too high for trapping to occur. Here, the transition between circulation and libration is unstable, such that resonant perturbations overpower the drift force. Accordingly, just like a pendulum flipping 180°, the body quickly crosses the resonant zone. Once across, the

resonant perturbations diminish in strength, allowing the drift force to dominate.

In our numerical integrations, meteoroids crossing a resonance boundary are seen to undergo rapid $\pm a$ changes, allowing these bodies to quickly advance to the opposite side of the resonance zone. Figure 10 shows several "jumps" associated with the three $(m_J, n_S, k) = (9, -6, -2)$ Jupiter–Saturn–asteroid resonances between 2.34 and 2.36 AU. In these cases, jumps occur regardless of whether the meteoroid is moving toward or away from Jupiter; presumably the evolution rate is swift enough that capture into such narrow resonances is not possible. These jumps are often accompanied by an increase in e.

Secular resonances, such as the ν_6, produce somewhat different phenomena. By definition, $[da/dt]_{res}$ is zero for a secular resonance. Thus, as long as $[da/dt]_{drift}$ is present, capture can not occur. Only jumps are possible. A numerical simulation (Vokrouhlický and Farinella 1998b), based on the perturbation equations, has found that the ν_6 secular resonance is ineffective for very high drift rates.

5.2. Meteoroids from 8 Flora

For our next set of Yarkovsky runs, we investigated debris from 8 Flora, a 140 km diameter S-type asteroid with osculating orbital elements $a = 2.202$ AU, $e = 0.156$, and $i = 5.89°$ (Chamberlin et al. 1997). Asteroid 8 Flora is the largest member of the Flora family, a group of asteroids with similar spectral features, proper eccentricities, and proper inclinations, possibly derived from a common precursor via a catastrophic collision (Zappalà et al. 1995). Since Flora family members dominate the population of objects between 2.1 and 2.3 AU (Cellino et al. 1991), and 8 Flora (and its family) is located within ~ 0.04 AU of the ν_6 resonance (Morbidelli and Gladman 1998), it is plausible that a significant fraction of terrestrial meteorites can be traced back to this family.

Starting our test bodies at the same site at 8 Flora, we again investigated the dynamical evolution of two sets of stony meteoroids, one having $K = 2.65$ W m^{-1} K^{-1}, the other with $K = 0.0015$ W m^{-1} K^{-1}. Other integration and meteoroid properties remained the same as those described for the 6 Hebe runs, except that A was increased slightly to 0.11 to remain consistent with 8 Flora (Chamberlin et al. 1997).

5.2.1. Flora meteoroids: Slow drift rate.
In the slower evolution case (i.e., $K = 2.65$ W m^{-1} K^{-1}), the maximum seasonal and diurnal da/dt rates are $\sim -8 \times 10^{-4}$ AU Myr^{-1} and $\sim \pm 5 \times 10^{-4}$ AU Myr^{-1}, respectively (no planetary perturbations). Note that these rates are faster than comparable Hebe-like meteoroids, since the particles start closer to the Sun. Turning planetary perturbations and collisions on, we find $\langle da/dt \rangle$ after 10 Myr is $\sim(-5.6 \pm 3.0) \times 10^{-4}$ AU Myr^{-1}, too slow to expect many meteoroids to enter the ν_6 resonance in 50 Myr.

Nearly all of the meteoroids reached MC orbits (i.e., 46 particles, or 92%) during the run, the mean time to reach such an orbit being 24.0 ± 8.5 Myr, while the mean position where they get these orbits is $\langle a \rangle = 2.1883 \pm 0.0049$ AU. Since the approximate position of the ν_6 resonance for Flora meteoroids is 2.16 AU, we suspect the Yarkovsky effect has dragged our meteoroids into other nearby resonances. Morbidelli and Nesvorný (1999) report that the 9 : 11 and 7 : 12 mean-motion resonances with Mars are in this region. Combined with the proximity of the ν_6 resonance (and perhaps a background of other high-order resonances), they make this region just chaotic enough to pump up e oscillations to MC orbits. Thus, Yarkovsky thermal forces and weak mean-motion resonances work together to deliver material to the MC region.

Once bodies have orbits that cross the orbital path of Mars, their evolution becomes characterized by abrupt changes in a owing to close encounters with Mars. Some of these a changes can deposit meteoroids deep into the ν_6 resonance; 4 of the 50 meteoroids reached EC orbits in this fashion. Most of the jumps, however, moved the objects away from the resonance. This trend, though perhaps not statistically significant, shows itself in the changing $\langle da/dt \rangle$ rate as we move from non-MC to MC epochs: $\langle da/dt \rangle$ goes from -5.6×10^{-4} AU Myr^{-1} (0–10 Myr) to -5.3×10^{-4} AU Myr^{-1} (10–20 Myr) to -4.8×10^{-4} AU Myr^{-1} (20–50 Myr). Recall that collisions are constantly changing the spin axes of the meteoroids, so preferential removal of fast-moving objects is unlikely to cause this trend.

5.2.2. Flora meteoroids: Fast drift rate.
In the fast-drift case (i.e., $K = 0.0015$ W m^{-1} K^{-1}), the maximum seasonal and diurnal da/dt rates are $\sim -2 \times 10^{-3}$ and $\sim \pm 2 \times 10^{-2}$ AU Myr^{-1}, respectively (no planetary perturbations). Including the planets and collisions, $\langle da/dt \rangle$ for the meteoroid swarm after 5 Myr of evolution is $\sim(-3.8 \pm 6.8) \times 10^{-3}$ AU Myr^{-1}. Thus, the ν_6 resonance is within easy reach of most particles during the integration. The low mean but large spread in $\langle da/dt \rangle$ is caused by diurnal drift, which allows bodies to move inward and outward at rates exceeding the seasonal component. Note that collision events, which randomize meteoroid spin axes, cause the statistical mean value of da/dt for an ensemble of bodies to decrease. In systems where collisions are frequent, a meteoroid's movement via the diurnal effect is transformed into a random walk, such that seasonal drag can sometimes dominate da/dt (regardless of the meteoroid's thermal conductivity K). The dispersion of the ensemble in a, however, may still be controlled by the diurnal effect. If the dispersion is large, and the mean change in a from the seasonal effect is small (e.g., the bodies are covered by regolith), the disperison will be the most important effect. If the dispersion in a is comparable to the distance to resonances like the 3 : 1 or ν_6, the diurnal effect will dominate the Yarkovsky leakage of bodies from the main belt.

A representative meteoroid evolution is shown in Fig. 12. We see that five spin axis reorientation events, represented by open circles, occur before the body enters the ν_6 resonance. Like the Hebe cases, e oscillations grow in amplitude as the meteoroid approaches the ν_6 resonance. A minor resonance-jumping event at 2.8 Myr (corresponding to the 7 : 12 mean-motion resonance
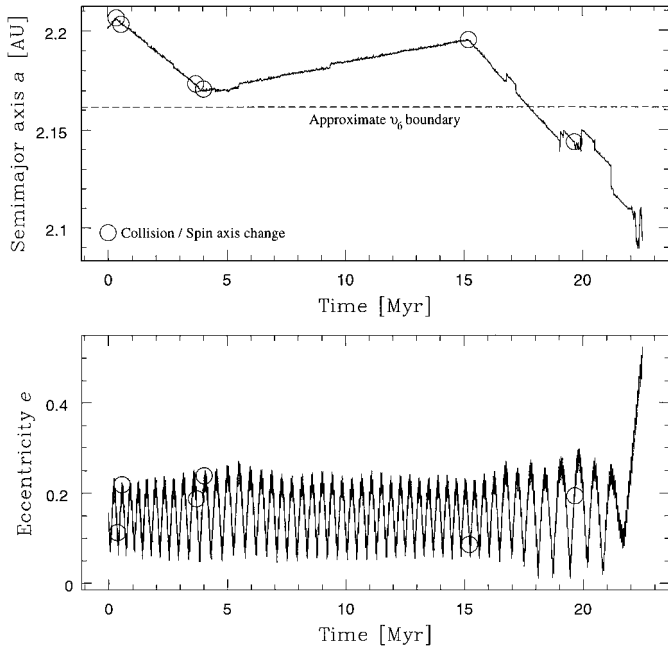
FIG. 12. Dynamical evolution of an $R = 1$ m Flora-like meteoroid. Starting orbit has $a = 2.202$ AU, $e = 0.156$, and $i = 5.89°$. Starting $\hat{b} = (0.307, -0.404, 0.862)$. Meteoroid properties are the same as in Fig. 9, except $A = 0.11$. Jumps in a are caused by encounters with various Mars and three-body mean-motion resonances. The longer-period e oscillations seen after 15 Myr are caused by the object's proximity to the ν_6 resonance.

with Mars) does not have much effect. The meteoroid is captured by the $10:17$ mean-motion resonance with Mars at ∼4 Myr shortly after a collision event; note the steady increase in the amplitude of e over ∼1.5 Myr as the body is prevented from approaching the ν_6 resonance. At 5.5 Myr, the body escapes and immediately moves outward. A second encounter with the $12:7$ Mars resonance produces a small jump but no major changes to a or e. Eventually, a collision at 15 Myr reverses the direction of the meteoroid's evolution, allowing it to approach the $10:17$ mean-motion resonance from the other direction. As it crosses this resonance, a increases and then decreases a short time later, producing a square-wave-like shape on the plot. As the body continues its inward evolution past this resonance, perturbations from the ν_6 resonance increase the period and magnitude of the e oscillations. Finally, a sequence of jumps, produced by a host of closely spaced three-body and Mars mean-motion resonances with $a \lesssim 2.15$ AU, combine with Yarkovsky drift to place the object deeply into the ν_6 resonance. From here, chaotic e variations from the ν_6 resonance quickly make the meteoroid an Earth-crosser. The elapsed time from start to finish is 22.49 Myr.

The evolution of all 50 Flora-like meteoroids in (a, e) space is shown in Fig. 13. The ν_6 resonance is positioned to correspond to meteoroids with a mean i between ∼5° and 6°. After 1 and 2 Myr of evolution, secular perturbations and the Yarkovsky effect cause the objects to spread in a and e, moving many of them closer to MC orbits and the ν_6 resonance. The 6-Myr

snapshot shows many objects in those regions, while the 7-Myr snapshot captures several objects en route to the EC zone (2 have already reached it, and 4 more will reach it by 8 Myr). The last two frames show the distribution after 20 and 50 Myr. Only 28 are left after 20 Myr, while just 16 remain after 50 Myr. It is clear that Flora meteoroids are well positioned to escape the main belt.

Forty-seven of the Flora clones became Mars-crossers (94%), while twenty-seven became Earth-crossers (54%). The shortest intervals needed for a particle to reach crossing orbits with Mars and Earth were 1.36 and 6.82 Myr, respectively. The median planet-crossing times for meteoroids with Mars and Earth were 2.87 and 16.18 Myr, while the mean crossing times were 8.1 ± 11.4 and 17.8 ± 10.4 Myr, respectively. Interestingly, the Earth times are not so different from the CRE ages of H-chondrites (Marti and Graf 1992, Graf and Marti 1995); see Discussion.
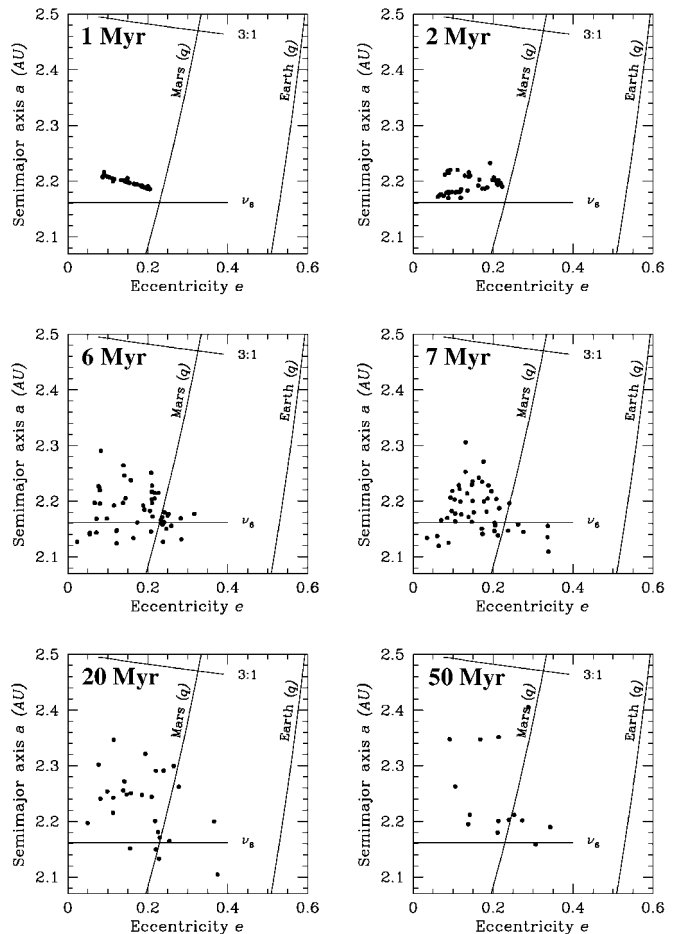
FIG. 13. Snapshots from the orbital evolution of 50 Flora-like meteoroids. Integration parameters, meteoroid sizes, and material properties are the same as in Fig. 11. Resonances and planet-crossing perihelia (q) values are shown. Meteoroids reaching Earth-crossing orbits are removed from the run. The meteoroid swarm is shown after 1, 2, 6, 7, 20, and 50 Myr of integration. Note that some objects reach Mars-crossing orbits before entering the ν_6 resonance.

5.3. Meteoroids from 170 Maria

For our next set of Yarkovsky runs, we investigated debris from 170 Maria, a 45-km diameter S-type asteroid with osculating orbital elements $a = 2.554$ AU, $e = 0.064$, and $i = 14.42°$ (Chamberlin *et al.* 1997). Asteroid 170 Maria is the largest member of the Maria family, a group of S-class asteroids just outside the 3 : 1 mean-motion resonance with Jupiter. The Maria family is smaller than several inner main belt families (e.g., Flora, Eunomia), but it is strategically located next to this main-belt "escape hatch," making it a good candidate to supply meteoroids and asteroids to the EC zone (e.g., Zappalà *et al.* 1997).

As before, test meteoroids with $K = 2.65$ W m^{-1} K^{-1} and $K = 0.0015$ W m^{-1} K^{-1} were studied. Other integration and meteoroid properties were kept the same as before, except the bond albedo which was set to Maria's estimated value ($A = 0.068$) (Chamberlin *et al.* 1997).

5.3.1. Maria meteoroids: Slow drift rate.

The maximum seasonal and diurnal da/dt rates, assuming no planetary perturbations, for the $K = 2.65$ W m^{-1} K^{-1} meteoroids were $\sim-5 \times 10^{-4}$ and $\sim\pm4 \times 10^{-4}$ AU Myr^{-1}, respectively. Integrating these particles for 50 Myr, we determined $\langle da/dt \rangle$ to be $\sim-3.4 \pm 1.2 \times 10^{-4}$ AU Myr^{-1}, half the speed needed to reach the 3 : 1 resonance (located $\Delta a = 0.036$ AU away). Since we are most interested in what happens to meteoroids that reach the 3 : 1 resonance, we leave this run to concentrate on the $K = 0.0015$ W m^{-1} K^{-1} results.

5.3.2. Maria meteoroids: Fast drift rate.

For this lower K value, the maximum seasonal and diurnal da/dt rates are $\sim-2 \times 10^{-3}$ and $\sim\pm2 \times 10^{-2}$ AU Myr^{-1}, respectively (no planetary perturbations). Including the planets and collisions, we find the resultant $\langle da/dt \rangle$ rate for the particles after 3 Myr of evolution (i.e., before they enter the 3 : 1 resonance) is $\sim(-1.1 \pm 6.5) \times 10^{-3}$ AU Myr^{-1}, fast enough for many particles to reach the 3 : 1 resonance within meaningful integration time.

The dynamical behavior of inward-drifting meteoroids encountering the 3 : 1 resonance was more unusual than we anticipated. Based on resonance-jumping events seen for Hebe- and Flora-like meteoroids in the inner main belt, we might have expected Maria-like meteoroids to jump the 3 : 1 resonance. Owing to the strongly chaotic dynamics that occur when the 3 : 1 resonance overlaps the ν_6 secular resonance (Morbidelli and Moons 1995), numerical simulations are needed to follow meteoroid behavior.

Figure 14 shows an example of a jump at the 3 : 1 resonance. Shortly after this meteoroid crosses the outer 3 : 1 resonance boundary (near 2.52 AU), it starts to undergo large a oscillations. The amplitude of one such oscillation is strong enough to move the meteoroid all the way to the inner boundary of the resonance (near 2.49 AU). At this point, the meteoroid's behavior is unpredictable; the wide separatrices of the 3 : 1 resonance mean that drifting bodies may or may not be able to complete the jump by leaping across the resonance's inner boundary. Our meteoroid, though, can be observed to move across the 3 : 1's inner bound-
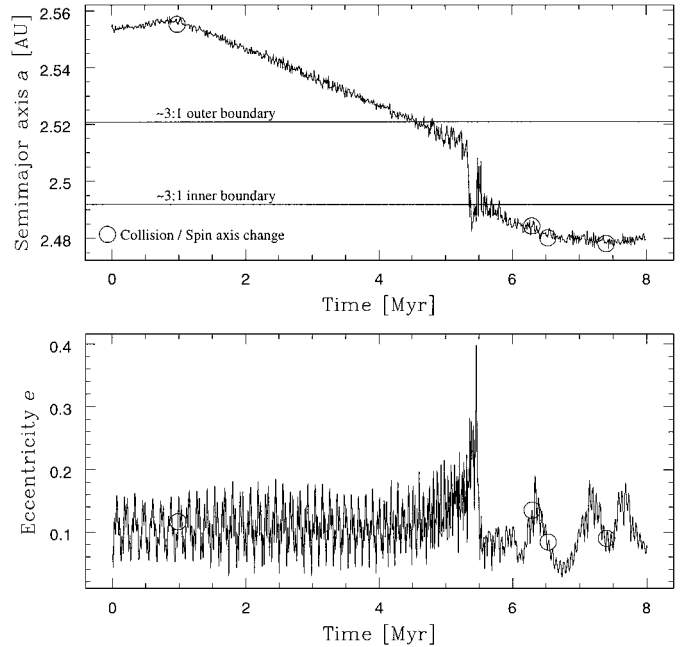
FIG. 14. Dynamical evolution of an $R = 1$ m Maria-like meteoroid. Starting orbit has $a = 2.554$ AU, $e = 0.064$, and $i = 14.42°$. Starting $\hat{b} = (-0.922, -0.044, 0.384)$. Meteoroid properties are the same as in Fig. 9, except $A = 0.062$. Note that the inward-moving meteoroid "jumps" across the 3 : 1 resonance and reaches its inner boundary. After some additional chaotic behavior, the object escapes. The long-period e oscillations seen after 6 Myr are caused by the object's proximity to the ν_6 resonance.

ary after ~0.5 Myr of chaotic a, e oscillations. Here, it becomes susceptible to long-period e oscillations from the ν_6 resonance (i.e., after 6 Myr of evolution). Thus, Yarkovsky forces allow some meteoroids to cross one of the strongest resonances in the inner main belt.

The evolution of all our Maria-like meteoroids in (a, e) space is shown in Fig. 15. The ν_6 resonance is positioned to correspond to meteoroids with a mean $i \sim 15°$. The first frame shows the meteoroids spreading after 1 Myr, while the second shows some meteoroids approaching the cusp of the 3 : 1 resonance (3 Myr). The next frame shows the evolution 1 Myr later; note that the two lowermost objects have undergone a resonant jump and will eventually evolve out of the 3 : 1 resonance via Yarkovsky drag. All meteoroids entering the 3 : 1's outer boundary undergo jumps to the proximity of the inner boundary, though only some escape, typically those with the fastest inward drift rates. At 10 Myr, 10 particles have been removed from the system, and 5 particles have escaped through the 3 : 1 resonance, while several others are preparing to jump or are in mid-jump. At 20 Myr, 21 particles have been removed from the system. Bodies that survived passage across the 3 : 1 resonance are heading for the ν_6 resonance. Note that the single meteoroid lying on the inner boundary of the 3 : 1 resonance is actually an escaped body from the 10-Myr frame; a collision reoriented its drift direction from inward to outward. Since resonance-jumping events at the 3 : 1 resonance for outbound bodies are rare, this object now reaches
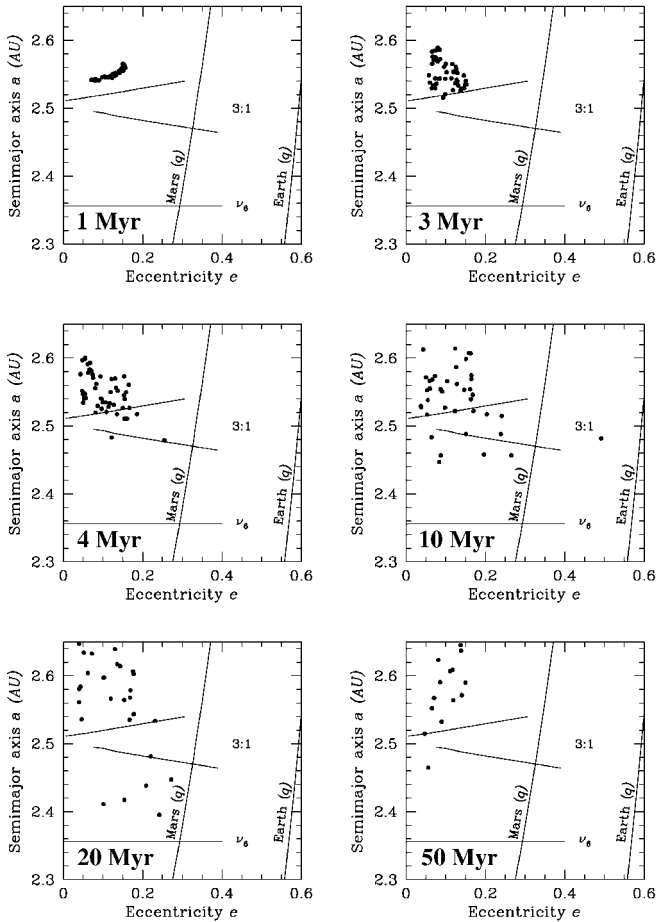
FIG. 15. Snapshots from the orbital evolution of 50 Maria-like meteoroids. Starting orbit, integration parameters, meteoroid sizes, and material properties are the same as in Fig. 13. Resonances and planet-crossing perihelia (q) values are shown. Meteoroids reaching Earth-crossing orbits are removed from the run. The meteoroid swarm is shown after 1, 3, 4, 10, 20, and 50 Myr of integration. Note the considerable number of objects that jump across the 3 : 1 resonance.

an EC orbit via the 3 : 1 resonance. Finally, the last frame shows the simulation after 50 Myr. The meteoroids that do remain (18 of them) mostly stayed away from the 3 : 1 resonance.

We found that 32 meteoroids (64%) crossed the 3 : 1 resonance's outer boundary during 50 Myr. Each of these bodies experienced some form of resonant "jump" that moved them to the proximity of the 3 : 1 resonance's inner boundary. From there, 12 bodies drifted out of resonance completely, and the other 20 lingered near the boundary long enough to get their e's pumped up to MC and EC orbits. Note that most of the 12 that drifted across the 3 : 1 resonance's inner boundary entered the ν_6 resonance, where they had a second chance to escape the main belt. In terms of overall statistical results, the same number of meteoroids that reached the 3 : 1 resonance also reached MC and EC orbits (32, or 64%). The shortest intervals needed for a particle to reach a crossing orbit with Mars and Earth were 4.57 and 4.81 Myr, respectively. The median planet-crossing times

for meteoroids with Mars and Earth were 11.37 and 15.3 Myr, respectively.

5.4. Additional Runs

We also tracked the meteoroid evolution from several other parent bodies in the inner main belt ($a < 2.8$ AU). The proper orbital elements for these sources are plotted in Fig. 9. No parent bodies were investigated beyond 2.8 AU, mostly because the 5 : 2 mean-motion resonance with Jupiter, located at 2.8 AU, is very efficient at increasing the orbital eccentricities of test bodies to Jupiter-crossing values, where these bodies are usually ejected from the Solar System. Morbidelli and Gladman (1998) have shown that only ∼1% of test bodies started in the 5 : 2 resonance reach orbits with $a < 2$ AU; most reach Jupiter-crossing orbits and are ejected from the inner Solar System. Unless it can be shown that the flux of main-belt material entering the 5 : 2 resonance is exceedingly high, we must conclude that most meteorites do not come from the outer main belt. Note that there may be other ways for outer main-belt material to reach Earth (e.g., meteoroids injected into $a < 2.8$ AU orbits, meteoroids dynamically "jumping" the 5 : 2 resonance and drifting into the 3 : 1 resonance).

The three runs described above (Hebe, Flora, and Maria) broadly characterize meteoroid evolution in the inner main belt. Meteoroids located between the ν_6 and 3 : 1 resonances behaved similarly to Flora-like meteoroids when i was low, and similarly to Hebe-like meteoroids when i was high. Meteoroids located between the 3 : 1 and 5 : 2 resonances behaved much like Maria-type meteoroids. For this reason, we do not describe the rest of our runs in the same detail as before. Four test parent bodies (e.g., 1 Ceres, 15 Eunomia, 44 Nysa, 4 Vesta) were chosen because they are the largest members of prominent inner main-belt asteroid families. We assert that meteoroid dynamical paths and time scales from these parent bodies are representative of evolution from other family members. The remaining parents (e.g., 13 Egeria, 19 Fortuna, 46 Hestia, 304 Olga) were chosen because their size and/or location suggests they may strongly contribute to the expected meteoroid flux entering the 3 : 1 or ν_6 resonances (e.g., Farinella *et al.* 1993).

All the results discussed below, presented in alphabetical order, were obtained using fast drift rates (thermal conductivity $K = 0.0015$ W m^{-1} K^{-1}). Albedo A values were chosen to correspond to the Bond albedo of each parent asteroid (Lebofsky and Spencer 1989). Asteroid data were provided by the Horizons On-line Ephemeris System v2.78 (Chamberlin *et al.* 1997). All other parameters were kept the same as before. Starting orbital parameters and outcome statistics are displayed in Table II.

5.4.1. 1 Ceres. The 1 Ceres, a G-type asteroid, is the largest asteroid in the main belt ($D = 933$ km), such that it is a big target for impactors and a potentially good source for ejecta. Ceres's orbital parameters (Table II), however, place it far from the 3 : 1 resonance (∼0.25 AU); average integration drift rates of $\langle da/dt \rangle = (-4.9 \pm 1.3) \times 10^{-2}$ AU Myr^{-1} are slow enough that

meteoroids must be long-lived to escape that way. For example, it takes 18 Myr in our run for the first Ceres-like meteoroid to reach the 3 : 1 resonance. In addition, those meteoroids that do make it are susceptible to jumping across the resonance.

A closer escape hatch is the 5 : 2 resonance, which only lies $\sim$0.05 AU away from Ceres. The proximity of this resonance explains why one of our meteoroids reached MC and EC orbits within 7 Myr (Table II), and why the average MC and EC times are only $\sim$23–25 Myr. As discussed above, though, the 5 : 2 resonance is an unlikely meteoroid source.

The 8 : 3 mean-motion resonance with Jupiter, located inside Ceres's orbit at 2.7 AU, may provide a third meteoroid escape route out of the main belt. Though most tested meteoroids drifting inward actually jump this high-order (and less powerful) resonance, our results show that three meteoroids had their e values pumped up by this resonance to barely MC orbits. At this point, the bodies lingered for several Myr before Mars pushed them to higher e values and an EC orbit. Future tests will determine whether the flux of material escaping via the 8 : 3 resonance is significant, and whether this material is likely to hit the Earth.

Overall, 44 and 34% of the meteoroids reached MC and EC orbits, but few of these bodies reached $a < 2$ AU orbits, not surprising given the nature of the resonances between 2.5 and 2.8 AU.

5.4.2. 15 Eunomia. Asteroid 15 Eunomia is the largest member ($D = 255$ km) of the Eunomia family (Zappalà *et al.* 1995), an S-class body located approximately 0.11 AU from the 3 : 1 resonance and 0.16 AU from the 5 : 2 resonance. Meteoroids evolving from this location have an integrated drift rate of $\langle da/dt \rangle = (-3.6 \pm 13) \times 10^{-3}$ AU Myr^{-1}, placing them within range of the 3 : 1, 8 : 3, and 5 : 2 resonances within 50 Myr.

Twenty-three meteoroids reached the 3 : 1 resonance during 50 Myr. Sixteen of the twenty-three (70%) crossed the 3 : 1 resonance's outer boundary and had their e's pumped up to EC values; the remaining seven (30%) jumped and exited the 3 : 1 resonance as they evolved inward. These values are comparable to the Maria outcomes described above. Two of the seven that escaped the resonance reversed direction after a collision event and reentered the 3 : 1 resonance across the inside boundary; resonant pumping of e allowed them to escape the main belt. Four meteoroids reached the 5 : 2 resonance before time elapsed, with three escaping via that route.

The fourth Eunomia-like meteoroid to reach the 5 : 2 resonance followed a very interesting dynamical path, displayed in Fig. 16. The orbital evolution can be characterized as follows: (i) Meteoroid moves steadily outward. Collision event at 5.7 Myr and passage across 8 : 3 resonance have no noticeable effect. (ii) Collision event at 9.34 Myr reverses the meteoroid's drift direction, allowing it to jump back across the 8 : 3 resonance. (iii) Third collision event at 12.86 Myr again reverses the meteoroid's drift direction, allowing it to encounter the 8 : 3 resonance yet again. (iv) At $\sim$13.8 Myr, the fast moving meteoroid ($b_x = -0.595$, $b_y = -0.084$, $b_z = 0.800$) is trapped by the 8 : 3 resonance. The duration of the capture is $\sim$2 Myr. The
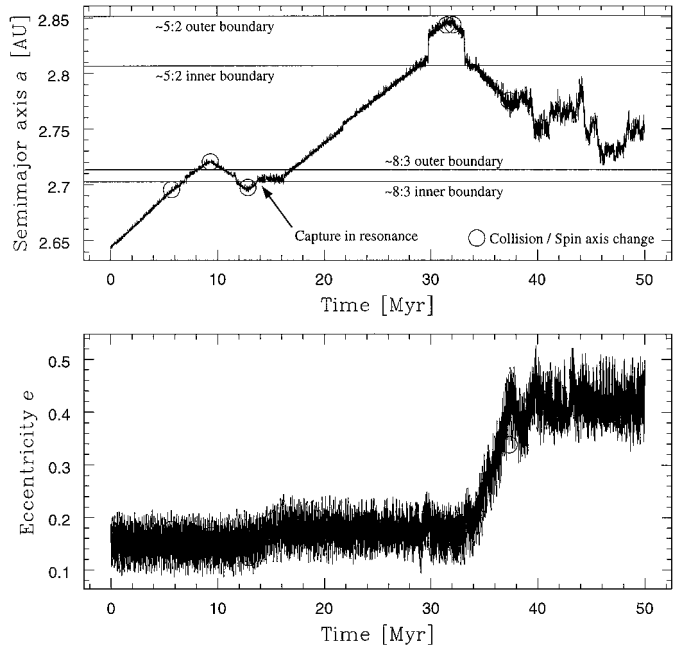
FIG. 16. Dynamical evolution of an $R = 1$ m Eunomia-like meteoroid. Starting orbit has $a = 2.643$ AU, $e = 0.187$, and $i = 11.76°$. Starting $\hat{b} = (-0.101, 0.534, 0.839)$. Meteoroid properties are the same as in Fig. 9, except $A = 0.094$. Interesting features in this evolutionary track are (i) 8 : 3 resonance jumping event near 12 Myr, (ii) 8 : 3 resonance capture event near 13 Myr, (iii) two 5 : 2 resonance jumping events, one outward, one inward, after 30 Myr.

body's mean e is moderately increased during this time. (v) The meteoroid escapes, jumps the $(m_J, n_S, k) = (3, -1, -1)$ Jupiter–Saturn–asteroid resonance at $a = 2.75$ AU, and travels to the 5 : 2 resonance. (vi) The meteoroid undergoes an outward jump to the 5 : 2 resonance's outer boundary, though it fails to escape. (vii) A collision at 32.13 Myr reverses the drift direction. The body jumps back to the 5 : 2 resonance's inner boundary. (viii) The meteoroid adheres to the resonance boundary while e is pumped up to MC values. (ix) At $\sim$38 Myr, the meteoroid is removed from the 5 : 2 resonance via a close encounter with Mars. Close encounters and passage into chaotic resonance regions dominate the remaining integration time, causing a to random walk. The conclusion we draw from this is that meteoroids often have unpredictable paths, and that collisions play a very important role in determining the ultimate outcomes for particular objects.

All of the Eunomia-like bodies that reached the 3 : 1 or 5 : 2 resonance became MC (27, or 54%), while a slightly smaller number became EC (21, or 42%). The mean MC and EC time for these bodies was $\sim$31 Myr. In terms of dynamical evolution, the biggest difference between this run and the Maria run appears to be Eunomia's starting osculating inclination ($i = 11.8°$), which was low enough to prevent meteoroids from approaching the ν_6 resonance after they jumped the 3 : 1 resonance.

5.4.3. 13 Egeria. Asteroid 13 Egeria is a 298-km G-type (i.e., a subclass of C asteroids) with orbital parameters comparable to those of 170 Maria (Table II). It is located

approximately 0.057 AU from the 3 : 1 resonance, small enough that it could be source of carbonaceous chondrites. We estimate that the mean drift rate for our Egeria-like meteoroids is $\langle da/dt \rangle = (-1.3 \pm 12) \times 10^{-3}$ AU Myr^{-1}, less negative than some other drift rates because of fortuitous $\hat{b}$ starting orientations (i.e., the particle distribution spread more-or-less equally inward and outward).

The overall evolution of the meteoroid swarm is very similar to that of the Maria-like meteoroids; after a few Myr of evolution, several bodies enter and then jump the 3 : 1 resonance. Those unable to completely escape the 3 : 1 resonance reach MC and EC orbits; the rest drift inward until they enter the ν_6 resonance. We found that the earliest MC and EC orbit times were 5.68 and 6.23 Myr, respectively, while the mean crossing times for the meteoroid distribution were 19.0 and 22.9 Myr, respectively. The overall fraction of bodies attaining planet-crossing orbits was higher for Egeria-like bodies than for Maria-like bodies (i.e., 74% became MC vs Maria's 64%; 70% became EC vs Maria's 64%).

5.4.4. 19 Fortuna. Fortuna is a 200-km G asteroid located approximately 0.32 AU from the ν_6 resonance and 0.045 AU from the inner boundary of the 3 : 1 resonance. For this reason, Fortuna, like Egeria, may be a good source of carbonaceous chondrites. In this case, however, Fortuna is located closer to the sun than the 3 : 1 resonance, such that the negative mean drift rate for our meteoroids ($\langle da/dt \rangle = (-3.0 \pm 13) \times 10^{-3}$ AU Myr^{-1}) moves the mean position of the swarm away from this escape route. Thus, we expect, on average, roughly half of the population or less to enter the 3 : 1 resonance in 50 Myr of integration time.

The first meteoroid to escape the 3 : 1 resonance reaches MC and EC orbits at 4.6 and 4.7 Myr, respectively. These crossing times are similar because the 3 : 1 resonance is very effective at pumping up e values. The earliest inward-evolving meteoroid becomes MC, however, in 18 Myr. Like the Flora-like meteoroids, e-pumping prior to entering the ν_6 resonance allows these bodies to reach MC orbits earlier than anticipated. The mean evolution times needed by the meteoroids to reach MC and EC orbits were 23 and 22 Myr, respectively, the former being slightly larger because several MC meteoroids did not reach EC orbits (48% vs 26%).

As an interesting aside, we single out the evolution of one Fortuna meteoroid that reached an MC orbit at 21.25 Myr while it was far from the 3 : 1 and ν_6 resonances ($a = 2.40$ AU) (Fig. 17). After undergoing a collision near 3.8 Myr, this object evolves outward until it reaches $a \sim 2.3977$, the location of the $(m_J, n_S, k) = (4, -2, -1)$ Jupiter–Saturn–asteroid resonance. This resonance captures the meteoroid; no da/dt changes are observed for nearly 16 Myr while e increases. Collision events taking place during the interim give the body a variety of new obliquity values (e.g., $\hat{b}_z$ is 0.60 at 13.9 Myr, −0.09 at 15.9 Myr, and 0.89 at 18.2 Myr), but none are capable of dislodging the body from the resonance. Apparently, the new drift rates are compensated by the resonant perturbations (i.e., the equality
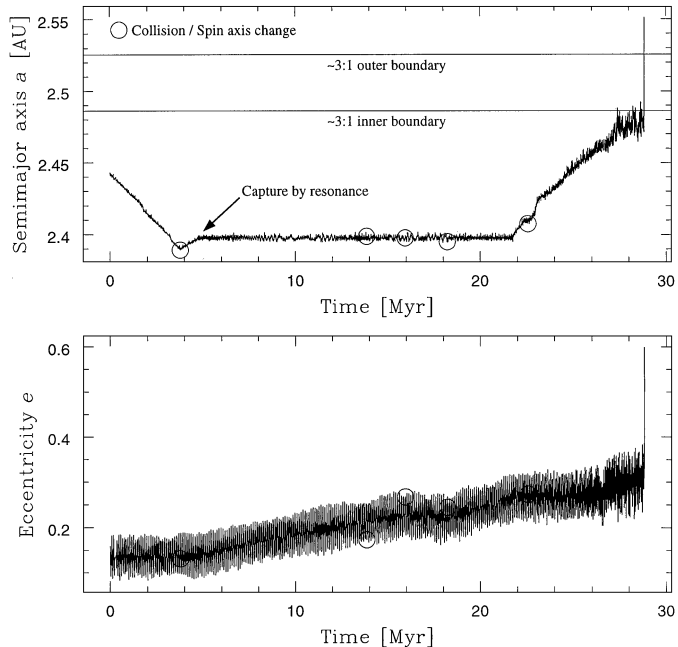
FIG. 17. Dynamical evolution of an $R = 1$ m Fortuna-like meteoroid. Starting orbit has $a = 2.443$ AU, $e = 0.159$, and $i = 1.57°$. Starting $\hat{b} = (-0.619, -0.214, -0.756)$. Meteoroid properties are the same as in Fig. 9, except $A = 0.035$. The interesting feature in this evolutionary track is a trapping in the $(m_J, n_S, k) = (4, -2, -1)$ Jupiter–Saturn–asteroid resonance (Nesvorný and Morbidelli 1998, Murray *et al.* 1998). The location of the resonance is at $a \sim 2.3977$ AU.

$[da/dt]_{\text{drift}} + [da/dt]_{\text{res}} = 0$ remains satisfied). In all likelihood, a stable libration would have continued until the limiting e value was reached. In this case, however, Mars close encounters free the object and Yarkovsky drift moves it to the 3 : 1 resonance, where it reaches an EC orbit. For more detail on capture processes, see Section 5.1.3.

Comparable captures have been noticed in other runs, though never in great enough number to signify a particular trend. We believe that frequent captures by narrow Jupiter–Saturn resonances are possible, though they will probably require smaller $[da/dt]_{\text{drift}}$ rates. Future work will explore how weak mean-motion resonances and the Yarkovsky effect work in tandem to deliver material to MC orbits.

5.4.5. 46 Hestia. Asteroid 46 Hestia is a 125-km P-class asteroid lying on the 3 : 1 resonance's outer boundary. Since this location guarantees minimal travel time for ejecta to reach the terrestrial-planet region, Hestia should be an excellent source for meteorites to the Earth. It is also possible that Hestia is the largest member of an asteroid family (Zappalà *et al.* 1995). Interestingly, no known meteorite type corresponds to P-type asteroid spectra. There are several plausible explanations for this discrepancy: (i) meteoroids from Hestia are too weak to survive passage through Earth's atmosphere; (ii) we are misidentifying the parent bodies of some meteorites; (iii) the contribution of Hestia ejecta to the overall flux of meteoroids reaching Earth is insignificant, either because the background population

is large or because very little debris is ejected at velocities greater than Hestia's escape velocity. Given that weak meteorites like carbonaceous chondrites survive to hit the Earth, and that extensive physical and chemical studies have been carried out on all meteorite classes, we suspect (iii) is probably true (or some combination of (i) and (iii)). Interestingly, new laboratory experiments indicate that hypervelocity projectiles shot into highly porous targets (40–60% bulk porosity) produce relatively few ejecta (Housen *et al.* 1999). This result may explain why 253 Mathilde, a porous C-type asteroid, has several huge undisturbed craters situated next to one another (Veverka *et al.* 1997). If Hestia is analogous to Mathilde, it might explain why such a large asteroid on the cusp of a dynamical pathway to Earth plays a tiny role in providing material to Earth.

The mean speed of our Hestia-like meteoroid after 1 Myr is $\langle da/dt \rangle = -6.3 \times 10^{-5} \pm 7.4 \times 10^{-3}$ AU Myr^{-1}. This value indicates that roughly equal numbers of meteoroids are moving inward and outward. Given the close proximity of the 3 : 1 resonance, it is not surprising to find that the earliest MC and EC times are only 1.14 and 1.15 Myr, respectively (i.e., the first meteoroid to enter the 3 : 1 resonance immediately had its e pumped up to EC values). Still, the mean MC and EC times for the meteoroid swarm are not much shorter than previous runs (9.9 and 12.0 Myr, respectively). This unexpected result is caused by meteoroids which first jump the 3 : 1 resonance and then return to reenter the resonance after a collision. Thirty-four of thirty-five (68%) bodies became MC as a result of interactions with the 3 : 1 resonance; the remaining particle became MC via the $(m_J, n_S, k) = (4, -2, -1)$ mean-motion resonance with Jupiter and Saturn. Thirty-two of the bodies perturbed by the 3 : 1 resonance also became EC (64%).

5.4.6. 44 Nysa. Asteroid 44 Nysa is a 70-km E-type and the largest component of the Nysa asteroid family, which may, in fact, be two independent overlapping families (Doressoundiram *et al.* 1998). Nysa's semimajor axis ($a = 2.423$ AU) places it moderately close to the 3 : 1 resonance (0.064 AU away), but its low inclination ($i = 3.7°$) places it far from the ν_6 resonance (0.29 AU away). These distances, and the fact that the mean drift speed of the meteoroids is negative and low ($\langle da/dt \rangle = (-2.0 \pm 4.2) \times 10^{-3}$ AU Myr^{-1}), imply that fewer bodies should reach the 3 : 1 and ν_6 resonance within 50 Myr of integration time than in other runs discussed so far.

For example, only seven Nysa-like meteoroids reach the 3 : 1 resonance; they end up being the only bodies to achieve EC orbits in this run. The mean time to become EC via this path is 25.3 Myr, with the earliest time being 10.33 Myr. Six more Nysa-like meteoroids become MC after drifting inward near or inside 2.2 AU, where they are perturbed by the multiplicity of resonances in this region. The mean time for these six bodies to become Mars-crossers is 41.4 Myr, raising the overall mean MC time for the thirteen bodies to 32.6 Myr. In addition, we find at least one Nysa meteoroid is temporarily captured for 14 Myr by the Mars 1 : 2 mean-motion resonance. During the first 10 Myr of capture, mean e increased from 0.18 to 0.23.

Then, after a collision changed $\hat{b}_z$ from 0.34 to 0.23, mean e began to decrease. When e reached 0.20, roughly 4 Myr later, the meteoroid escaped the Mars 1 : 2 resonance.

5.4.7. 304 Olga. Asteroid 304 Olga is a 68-km C-class asteroid adjacent to the nominal border of the ν_6 resonance and within 0.08 AU of the 3 : 1 resonance. Its proximity to these two strong resonances potentially makes Olga a very good source of material to Earth. Numerical modeling bears this out; we find that 92% of all of Olga meteoroids reach EC orbits (mean crossing time of 17.8 Myr) while 98% reach MC orbits (mean crossing time of 11 Myr). The first object to reach an EC orbit, however, takes 4.49 Myr, comparable to values from other parent asteroids. Note that the integrated drift speed for the distribution after 3 Myr ($\langle da/dt \rangle = (-9.3 \pm 88) \times 10^{-4}$ AU Myr^{-1}) is small enough to indicate that Olga-like meteoroids travel inward and outward with similar numbers and speeds.

The closeness of Olga to the ν_6 resonance would seem to downplay the role of weaker resonance phenomena, but even here we find that the 4 : 2 : 1 Jupiter–Saturn resonance ($a = 2.3977$) helps to pump up e values of five meteoroids to MC values. This effect does not significantly change the overall evolution of these meteoroids, but it does show that bodies with Olga-like orbits have several effective ways of leaving the main belt.
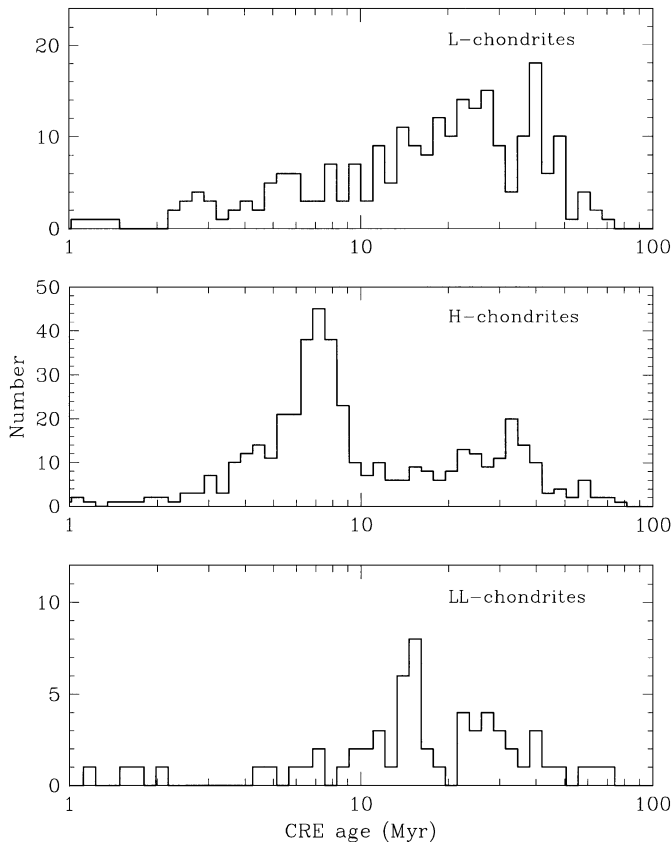
5.4.8. 4 Vesta. Asteroid 4 Vesta is a 510-km V-class asteroid with singular spectral features linking it to the "Vestoids," a number of sub-10-km asteroids thought to be Vesta ejecta (Binzel and Xu 1993), and the howardite, eucrite, and diogenites (HED) meteorites. It is located far from both the ν_6 resonance (0.18 AU) and the 3 : 1 resonance (0.13 AU), such that evolution times via the Yarkovsky effect may be lengthy. For our runs, the mean speed of the bodies after 10 Myr is $\langle da/dt \rangle \sim (-5.7 \pm 54) \times 10^{-4}$ AU Myr^{-1}, slow enough to suggest that only the extremes of the particle distribution make it to the major resonances before 50 Myr has elapsed. This long travel time, however, may be consistent with the observed CRE ages of the HED meteorites. More will be said about this in the discussion section.

The earliest Vesta-like meteoroid to reach MC and EC orbits arrives within ~14 Myr (via the 3 : 1 resonance). We find that a few bodies become temporarily trapped in minor resonances (e.g., $(m_J, n_S, k) = (4, -2, -1)$ Jupiter–Saturn–asteroid resonance or Mars resonances inside 2.2 AU), but these capture events do not appear to significantly change the mean MC and EC time scales (29.6 and 31.7 Myr, respectively). Only 36% of the meteoroids reach EC orbits within 50 Myr; the rest are left stretched between the ν_6 and 3 : 1 resonances.

6. DISCUSSION

6.1. Comparisons with Meteorite Cosmic-Ray Exposure Ages

Meteorite CRE ages are believed to measure the length of time the body spends between its final reduction in size by

FIG. 18. The number of meteorites vs cosmic-ray exposure age for L, H, and LL chondrites. Some minor clumping in the H and LL distributions is caused by multiple falls. Figure from Morbidelli and Gladman (1998). Data provided by T. Graf.

radiation on its immediate precursor before being liberated in an impact event). Thus, meteorites with short CRE ages may, in fact, have transit times as long as other meteorites (Graf and Marti 1995, Herzog *et al.* 1997). For this reason, it is difficult to support a scenario where many meteoroids are immediately injected into chaotic resonances with short terrestrial delivery times (e.g., 3 : 1 resonance), since that would create a preponderance of short CRE ages (Gladman *et al.* 1997). This result is a primary reason we chose to investigate the Yarkovsky effect in detail.

Interpretation of the features in the CRE-age histograms can be complicated, since we are only looking at a (biased) snap-shot of the CRE ages taken among "today's" EC meteoroids. For example, suppose 6 Hebe was hit by an asteroid 10 Myr ago, and that impact created a swarm of new meteoroids. Even if these meteoroids started reaching Earth within a few Myr, we would only know about those which hit and were protected by the Antarctic ice over the last 10^4–10^6 years. Thus, like barometers, CRE-age histograms tell us current conditions but not how the "weather" is changing. Unless we discover a cache of fossil meteorites, we cannot specify trends in the flux of material reaching Earth or constrain how the orbital distribution of the meteoroid swarm changes with time. Another issue hindering interpretation of the CRE-age histograms is the fact that some EC meteoroids are more likely to hit the Earth than others. Understanding how the orbital distribution of EC meteoroids from different parent bodies changes with time is critical to deciphering CRE-age histograms. Finally, meteorite survivability creates a strong bias in the meteorite record (e.g., the paucity of long-lived carbonaceous chondrites). Sticking to comparisons between similar meteorites appears to be the best way to deal with this problem.

Given these issues, and the fact that our test meteoroids were started with zero ejection velocities, we compare our results to CRE age data with some trepidation. Still, we can make some useful comments once we better understand how meteoroid evolution in the inner Solar System works. The best study of this issue to date is provided by Morbidelli and Gladman (1998), who have used numerical simulations to estimate how the collision probability between the Earth and individual meteoroids started in ν_6 and 3 : 1 resonances will change with time. Their results show that the meteoroids which go on to strike the Earth from these sources have a ~25% chance of doing so within 3–4 Myr, a 50% chance of doing so within 9–10 Myr, and a 75% chance of doing so within 22–25 Myr. Thus, if the ordinary chondrite population in the inner Solar System is in steady state, direct injection of chondrites into the ν_6 and 3 : 1 resonances would produce too many short CRE ages to match Fig. 18.

Even if a steady state exists at some level, it is possible that bursts of material produced by large main-belt impact events could intermittently flood the inner Solar System with meteorites (Zappalà *et al.* 1998). Potentially, these meteoroid swarms, if they live long enough, could create some of the CRE-age spikes seen in Fig. 18. To determine how the CRE-age histograms should be interpreted, we turn to "time-of-fall" statistics, which

impact, which places its entire interior within a few meters of the radiation environment, and delivery to Earth. Figure 18 shows meteorite number vs CRE age for L, LL, and H chondrites. From these data, the mean exposure ages of the L, LL, and H chondrites are 22, 20, and 14 Myr, respectively. Peaks are seen in each data set, ~7–8 and ~33 Myr for H-chondrites, ~28 and ~40 Myr for L-chondrites, and ~15 Myr for LL-chondrites. It is hypothesized that each peak might represent material from a large collision event. In fact, Marti and Graf (1992) argue that the histograms are dominated by stochastic events rather than a continuous meteoroid supply, such that the histograms cannot be satisfactorily fit by bell-shaped curves. On the other hand, Fig. 18 may just represent a smooth continuum which is poorly sampled. For example, the ~7–8 Myr H-chondrite peak may be produced by two events, one involving H5 chondrites, and a second involving the H3/4/6 chondrites (e.g., Morbidelli and Gladman 1998). Given this ambiguity, we will discuss the implications of both possibilities below.

Figure 18 shows that few chondrites have short CRE ages. When this meteorite subset is studied (CRE ages <4 Myr), many are found to have complex exposure histories, which occur when the CRE geometry changes (i.e., the meteorite is exposed to

measure the time of day when a meteorite strikes the Earth. Time-of-fall statistics provide information about meteoroid orbital trajectories and perihelion distances (q); meteorite falls during PM hours must come from bodies having $q \sim 1$ AU, while meteorite falls during AM hours must come from $q < 1$ AU. Numerical simulations of test bodies evolving out of the ν_6 and $3:1$ resonances indicate that $q \sim 1$ AU values generally come from dynamically young objects, while $q < 1$ AU values come from dynamically older objects that have had time to reach deep EC orbits (Morbidelli and Gladman 1998). Accordingly, since $\sim$68% of ordinary chondrite falls have been observed in the PM (Graf and Marti 1995), it is believed that the majority of ordinary chondrites have only been on EC orbits for a few Myr. This makes the Yarkovsky effect rather than long-lived meteorite swarms the leading candidate to explain most CRE-age spikes.

If this chain of logic holds, the time scales shown in Table II may be surprisingly close to the time scales needed to bring meteoroids to Earth. For example, to estimate meteoroid delivery time scales from main-belt parent bodies to Earth, we need to modify our runs to account for (a) non-zero ejection velocities and (b) evolution in the inner Solar System. If the time reduction due to (a) is roughly equivalent to the additional time required by (b), Table II results should roughly approximate the actual delivery times. For example, few of our fast-drifting meteoroids reach EC orbits before $\sim$5 Myr have elapsed, consistent with Fig. 18. In addition, meteoroids from prospective chondritic parent bodies (e.g., 6 Hebe, 8 Flora) have mean EC times ($\pm 1\sigma$) that overlap the major peaks of the H, L, and LL chondrites (Table II).

Comparable studies can be made using HED meteorites, which are believed to come from the the Vestoids or directly from Vesta itself. Welten *et al.* (1997), using 11 howardites, 32 eucrites, and 20 diogenites, find the CRE-age histogram of the HED meteorites to be similar to that of the ordinary chondrites: median ages are $\sim$20 Myr, maximum ages are $\sim$80 Myr, and a paucity of ages exist with <10 Myr. In addition, Welten *et al.* claim that these exposure ages are not randomly distributed; 23 HEDs cluster between 21 and 25 Myr, 10 between 35 and 42 Myr, and 8 between $\sim$12 and 13 Myr. For the first two groups, all three HED components are represented. For the last group, the eucrites and diogenites are represented, though there are not enough members to consider this sample statistically significant. Still, these three age-clusters comprise 55% of the howardites, 59% of the eucrites, and 80% of the diogenites, and they suggest at least two major impact events occurring $\sim$22 and 39 Myr ago. Welten *et al.* claim that 3–8 additional impact events in the last 50 Myr could conceivably explain all the known HED meteorites on Earth. Other studies of this issue, however, suggest that the HEDs may only be marginally in disagreement with a continuous meteoroid injection model which includes factors like meteoroid disruption and/or the Yarkovsky effect (Migliorini *et al.* 1997b).

An examination of our Vesta results from Table II indicates that our Vesta-like meteoroids have mean EC time scales within

1σ of these peaks (i.e., 31.7 ± 9.0 Myr), though we caution that our value may be biased by the length of our integration (50 Myr). Our earliest EC meteoroid, however, takes 15.35 Myr, longer than some of the younger HED meteorites. The problem might be alleviated by invoking a reasonable ejection velocity from Vesta or by assuming that Vestoids near a chaotic resonance provide a significant amount of material to EC orbits. We will look into this issue in greater detail below.

In summary, we conclude that our suggested $\langle da/dt \rangle$ rates and the meteoroid delivery times listed in Table II provide a reasonable scenario for explaining the distributions of CRE ages for stony meteorites.

6.2. Meteorite Parent Bodies: Small or Large?

An important implication of the Yarkovsky scenario is that high ejection velocities are no longer necessarily required to deliver meteoroids from nearly any parent body in the inner main belt to the $3:1$ or ν_6 resonances. (Note that we ignore the possibility of meteoroid delivery via Mars or three-body mean-motion resonances for now.) If fast Yarkovsky drift rates are the rule, meteoroids can evolve directly from their parent bodies to resonant "escape hatches" before disrupting. If slower Yarkovsky drift rates are common, meteoroids can ride a long way aboard larger precursors, which have faster seasonal drift rates (e.g., Fig. 4) but also longer collisional lifetimes. When this material is eventually exposed to cosmic rays, it presumably will be within range of a chaotic resonance that can take the meteoroid to Earth within a few tens of Myr. The latter scenario is analogous to the classical "collisional cascade" mechanism suggested previously (e.g., Wetherill 1985), with residence and collisions now taking place in the main belt rather than in the near-Earth region. Preliminary modeling of this scenario may be of some use in explaining the observed CRE ages of stony meteorites (Vokrouhlický and Farinella 2000).

Since all asteroids are now potential meteoroid parent bodies, we need to reexamine which asteroids are most likely to contribute meteorites to the Earth. Factors to consider are: (1) impact rate on parent body; (2) mass and velocity distribution of ejecta, which determines the escape fraction and the distance between parent body and escape hatch (e.g., $3:1$ resonance, ν_6 resonance, weak mean-motion resonance placing material on MC orbits from whence it is delivered, etc.); (3) Yarkovsky drift rate for ejecta; (4) ejecta disruption rate, (5) efficiency of transportation route in producing Earth-crossers; (6) dynamical lifetime of fragments; (7) terrestrial impact rate of meteoroids on various orbits; (8) meteoroid survivability issues (e.g., passage through atmosphere, surface erosion); and (9) discovery biases.

A key parameter affecting meteoroid flux (factors 1 and 2) is asteroid size. Big objects, with large geometric cross sections, are more frequently hit by other asteroids and thus may provide a greater flux of material than small asteroids. A possible counter to this effect is that big objects also have substantial escape velocities, such that they reaccumulate slow-moving ejecta. Small objects, which are numerous and have tiny escape velocities,

lose practically all their ejecta every time they are struck by an asteroid. To clarify which size produces more meteoroids, we perform the following calculation similar to those found in Greenberg and Chapman (1983) and Farinella *et al*. (1993).

The erosion rate of a target asteroid can be estimated as (Geissler *et al*. 1996)

$$\frac{dm}{dt} = P_i R^2 \rho \int_{r_{\min}}^{r_{\max}} \frac{dN(r)}{dr} V(r) \, f_{\mathrm{esc}} \, dr, \qquad (47)$$

where P_i is the intrinsic collision probability for the target (e.g., Bottke *et al*. 1994; note that P_i includes the factor π), R^2 is the target radius squared, ρ is asteroid density, $N(r)$ is the number of projectiles of radius r, $V(r)$ is the volume of material excavated by the projectile of radius r, and f_{esc} is the fraction of ejecta escaping after impact by a projectile of radius r.

We assume that the number of projectiles in the main belt in radius range r to $r + dr$ is

$$dN(r) = K r^{-b} \, dr \qquad (48)$$

with K a constant and b an exponent (e.g., Dobrovolskis and Burns 1984). To get f_{esc}, we turn to laboratory experiments, which suggest that ejecta fleeing an impact site always attain velocities greater than a cutoff value (v_c), and that the proportion of mass exiting a crater in excess of a given velocity is an inverse function of that velocity: ($f \sim v^{-k}$; $k \approx 9/4$) (e.g., Gault *et al*. 1963, Stöffler *et al*. 1975, Greenberg *et al*. 1978, Dobrovolskis and Burns 1984). Now, as long as the target asteroid's escape velocity $v_{\mathrm{esc}} > v_c$, $f_{\mathrm{esc}} \sim v_{\mathrm{esc}}^{-9/4}$. Since $v_{\mathrm{esc}} \propto R$, the fraction of ejecta that escapes is $f_{\mathrm{esc}} \propto R^{-9/4}$. If $v_{\mathrm{esc}} < v_c$, as it might be in the case of small targets, $f_{\mathrm{esc}} = 1.0$. Finally, we assume that crater volume is

$$V(r) = h r^3 \qquad (49)$$

for some constant h which depends on target material properties and impact velocity.

Substituting these values, dropping constants and small terms, and assuming that the largest projectile $r_{\max} \propto R$, we find that

$$\frac{dm}{dt} \propto R^{3.75 - b} \qquad (50)$$

for large bodies ($v_{\mathrm{esc}} > v_c$) and

$$\frac{dm}{dt} \propto R^{6 - b} \qquad (51)$$

for small bodies ($v_{\mathrm{esc}} < v_c$).

We will use these equations below to estimates the relative contribution to the meteoroid flux from variously sized asteroids. First, though, we need to estimate v_c, which will tell us at what size we transition from "large" to "small" asteroids. The value v_c can be estimated from laboratory experiments: $v_c = 50 \text{ m s}^{-1}$ for "hard" basaltic targets while $v_c = 1 \text{ m s}^{-1}$ for "soft" sand targets (Gault *et al*. 1963, Stöffler *et al*. 1975). To turn these

values into an asteroid size, we assume $v_c = v_{\mathrm{esc}}$, and

$$v_{\mathrm{esc}} = 120 \text{ m s}^{-1} (R/100 \text{ km}), \qquad (52)$$

corresponding to $\rho = 2500 \text{ kg m}^{-3}$ (Farinella *et al*. 1993). Substituting and solving for R, we find that the largest asteroid which can still lose all its ejecta is between $R = 0.83$ km (sand) and 42 km (basalt). Since images of Gaspra ($R \sim 7$ km; Belton *et al*. 1994) show that it has retained substantial amounts of regolith, and impacts in the gravity-scaling regime are more accurately modeled in the laboratory by weak sand targets, we believe that the lower end of the size range should be used.

To test our ideas, we apply our equations to the two possible sources of the HED meteorites, 4 Vesta ($R = 255$ km) and the observed Vestoids (e.g., Binzel and Xu 1993). For the latter, 43 main belt objects are now known to have V-type spectra, with mean and median radii $R \sim 5$ km. Assuming that the main belt asteroids are in collisional equilibrium ($b = 3.5$; Dohnanyi 1969) and that both Vesta and the Vestoids are in the $v_{\mathrm{esc}} > v_c$ category, we estimate that Vesta produces 2.7 times more ejecta than a typical Vestoid. Since there are many more Vestoids than Vesta, many of which reside near the 3 : 1 or v_6 resonances, this b value suggests that the Vestoids are a more important source of HEDs than Vesta itself. Note that if the typical Vestoid were in the $v_{\mathrm{esc}} < v_c$ regime while Vesta itself stayed in the $v_{\mathrm{esc}} > v_c$ regime, a single Vestoid would produce 14 times more ejecta than Vesta.

A more sophisticated treatment of the main-belt size distribution, however, yields a different result. Jedicke and Metcalfe (1998) have used debiased observational data from Spacewatch to estimate the size distribution of main-belt asteroids larger than 1 km. Their results showed that no single power-law exponent represents the main-belt size distribution. (Note that Cellino *et al*. (1991) arrived at the same conclusion using the IRAS database.) Follow-up work by Durda *et al*. (1998) showed there are two broad "humps" in the main belt size distribution, one between 3 to 30 km diameter bodies and another between 30 to 300 km diameter bodies. The transition region between the humps, however, has a shallow slope ($b \sim 1.4$). This "wave" pattern is expected to repeat itself; Durda *et al*. (1998), using a sophisticated collisional model, showed that there should be an extended transition region at sub-km sizes after the 3- to 30-km hump. If this sub-km region has a slope comparable to that of the transition region near 30 km, we predict that projectiles striking Vesta would produce (255 km/5 km)$^{3.75-1.4} \sim 10,000$ times more ejecta than a typical Vestoid for the $v_{\mathrm{esc}} > v_c$ regime. A more conservative slope index value ($b = 2.343$), derived from a weighted least-squares fit of Palomar–Leiden Survey data (Van Houten *et al*. 1970, Durda *et al*. 1998), suggests that Vesta may produce ~ 250 times more ejecta than a typical Vestoid. Either way, unless there are a large number of undetected multi-km Vestoids, these results indicate that the HED meteorite flux may be dominated by material from Vesta itself.

There may be additional support for low b values; preliminary work suggests that 1- to 10-m body disruption time scales,

estimated using the sub-km size-frequency distribution predicted by Durda *et al*. (1998), are too short to match meteorite CRE ages unless there are fewer projectiles than predicted by a Dohnanyi-type collisional equilibrium (R. Greenberg 1999, personal communication). A high flux of material from Vesta would also satisfy constraints provided by the HED meteorites, provided these meteoroids are supplied by intermittent impact events (e.g., Welten *et al*. 1997): (i) CRE-age peaks are more easily explained by stochastic impacts on a single source, like 4 Vesta, than by impacts on multiple Vestoids. For reference, Welten *et al*. has estimated that a 5- to 6-km Vestoid should be struck by a 20-m body every 10 Myr, while Vesta itself should be struck by a ∼2-km asteroid over the same time scale (note that both collision rates assume a slope parameter of $b = 2.0$). (ii) Individual Vestoids may not be composed of representative samples of all three HED constituents. This would make it difficult for them to reproduce the ∼22- and ∼38-Myr CRE age peaks with stochastic impacts. (iii) Even if some Vestoids do have a mixed composition, it is unlikely that all three HED constituents lie adjacent to one another on a 5- to 6-km body. Thus, a 20-m projectile striking a typical Vestoid would be unable to eject all HED constituents simultaneously.

Based on these results, we believe that peaks seen in the chondrite and HED meteorite CRE age histograms, if not produced by incomplete sampling, are best explained by stochastic impacts. We have shown that the Yarkovsky effect, in conjunction with voluminous ejection events from large parent asteroids, can be used to explain such CRE peaks. We caution, however, that long-lived meteoroid populations in the inner main belt could also explain some peaks. Finally, we point out that the Flora asteroid family, containing a good mix of large and small bodies with S-class spectral properties, is on the periphery of several transportation routes to Earth (e.g., ν_6 resonance, multiple Mars, and three-body mean-motion resonances). For this reason, the Flora family should provide a substantial contribution of similar-looking meteorites to Earth. We suspect this source may partially explain why so many meteorite falls and finds are ordinary chondrites.

6.3. Future Work

So far, we have used the YS code to model the dynamical evolution of (mostly) fast-moving meteoroids. This was done for practical considerations; meteoroids can take a long time to reach interesting places if slow meteoroid drift rates are used. Computational limitations also prevent us from exploring all possible thermal and physical parameters. Still, using reasonable parameters, we have demonstrated how planetary perturbations and Yarkovsky drag work together, and that our numerical results can satisfactorily match CRE-age data. In this section, we highlight several problems of interest that we hope to explore with the YS code in the future.

The meteoroids tested here sampled a range of $\hat{b}$ positions and drift speeds. We found that resonance-jumping and trapping mechanisms are affected by these drift rates; diagnostic tests will be needed to determine which drift rates cause particular effects. Studies of Yarkovsky drift in conjunction with high-order resonance phenomena should not only be useful to meteoroid delivery scenarios but also to near-Earth asteroid production scenarios. Recall that km-sized objects undergo small but significant Yarkovsky drift rates. It is possible that these bodies become trapped in Mars and Jupiter–Saturn resonances long enough to reach MC and eventually EC orbits. Thus, the Yarkovsky effect may be an important mechanism in resupplying the NEO population with km-sized material (Farinella and Vokrouhlický 1999). Another potentially important effect is resonance-jumping of outer main-belt material. If the flux of material near the 5 : 2 resonance is high enough, and meteoroids/immediate precursors can survive long enough, resonance-jumping may allow some outer main-belt material to reach the inner main-belt escape routes (possibly via a collisional cascade).

Because the intensity of Yarkovsky thermal forces depends on heliocentric distance, we also intend to test how thermal forces alter dynamical evolution among small bodies in the terrestrial planet region. For example, Mars ejecta, evolving under the Yarkovsky effect, may more readily reach inner Solar System resonances (and EC orbits) than previously estimated (e.g., Gladman 1997, Rubincam 1998). Meteoroids, already acting under the influence of close encounters and chaotic resonances, will undergo additional changes from Yarkovsky thermal forces. The implication of this additional force is not clear; the small-body population will become stirred to some unknown degree, with some objects being dragged into the Sun. Even km-sized asteroids approaching the Sun should undergo small but measurable a changes (e.g., 1566 Icarus; D. Vokrouhlický 1999, personal communication).

Other problems involving the Yarkovsky effect include (i) modeling the dynamical evolution of Trojan and Kuiper-belt bodies, (ii) determining whether Yarkovsky thermal forces are really responsible for an apparent "overabundance" of 10-m bodies in the NEO region (Rabinowitz *et al*. 1993, Rabinowitz 1994, Bottke *et al*. 1996), (iii) modeling the main-belt "collisional cascade" together with planetary perturbations and Yarkovsky drift forces, and (iv) modeling how the preferential removal of small bodies creates a feedback loop that changes the size-distribution of larger asteroids. Potential YS code improvements include better descriptions of how collisions modify spin axes and drift rates with time, more accurate estimates of meteoroid thermal properties, and refinements to the theoretical description of the Yarkovsky thermal forces to better account for high-e orbits.

7. SUMMARY OF RESULTS

We briefly summarize our results from this paper:

• We have formulated the seasonal and diurnal Yarkovsky thermal forces which modify the semimajor axes of bodies smaller than 10 km.

- These forces have been incorporated into the "swift-rmvs3" integrator. Tests verify that the hybrid "YS" code is working accurately, with benchmark meteoroid evolution runs from other groups exactly reproduced.

- Runs completed without planetary perturbations show that small meteoroids can undergo large inclination changes. Inclusion of planetary perturbations eliminate these changes, primarily because nodal precession causes Yarkovsky forces to destructively interfere over time.

- The evolutions of meteoroids (with different thermal properties) were tracked from several inner main-belt asteroids all the way to EC orbits. Our results show that most meteoroids from these asteroids reach EC orbits via the $3:1$ mean-motion resonance with Jupiter or the ν_6 secular resonance after tens of Myr of evolution.

- Most meteoroids attain MC orbits well before entering the $3:1$ or ν_6 resonance. Chaotic effects produced by weak resonances (e.g., mean-motion resonances with Mars, three-body resonances) appear to be responsible.

- Meteoroids drifting away from a planet producing a mean-motion resonance often jump the resonance. Meteoroids drifting toward the planet producing an isolated mean-motion resonance can be, with the right drift rate, trapped by that resonance. Captures in weak mean-motion resonances in the inner main belt can lead to increased e values, possibly pushing these objects onto MC orbits. If capture fails, the meteoroid jumps the resonance. Jumping events allow objects with $a > 2.5$ AU to potentially bypass the $3:1$ resonance.

- The evolution time scales for the meteoroids tracked here are consistent with the observed CRE ages of chondrites and HED meteorites (e.g., tens of Myr) as well as with the paucity of meteorites with CRE ages <10 Myr. Comparable tests indicate that the Yarkovsky effect can also explain very long CRE ages (0.1–1.0 Gyr) of iron meteorites, but disruption time scales are important.

- The contribution to the meteoroid flux from big and small parent bodies depends on the size-frequency distribution of the main belt. If the projectile population is in collisional equilibrium at sub-km sizes (i.e., an incremental power-law exponent of $b = 3.5$; Dohnanyi 1969), small asteroids are likely to provide the dominant share of meteoroids to the inner Solar System. On the other hand, if the projectile population making large craters on parent bodies has a shallow slope (Cellino *et al.* 1991, Durda *et al.* 1998), the largest main-belt asteroids (e.g., Vesta) will dominate the meteoroid flux. Spikes in the CRE data from the HED meteorites are more easily explained by impacts on Vesta than by multiple impacts on one or more Vestoids.

REFERENCES

Afonso, G. B., R. S. Gomes, and M. A. Florczak 1995. Asteroid fragments in Earth-crossing orbits. *Planet. Space Sci.* **43**, 787–795.

Belton, M. J. S., J. Veverka, P. Thomas, P. Helfenstein, D. Simonelli, C. Chapman, M. E. Davies, R. Greeley, R. Greenberg, and J. Head 1992. Galileo encounter with 951 Gaspra—First pictures of an asteroid. *Science* **257**, 1647–1652.

Binzel, R. P., and S. Xu 1993. Chips off of asteroid 4 Vesta—Evidence for the parent body of basaltic achondrite meteorites. *Science* **260**, 186–191.

Bottke, W. F., M. C. Nolan, R. Greenberg, and R. A. Kolvoord 1994a. Velocity distributions among colliding asteroids. *Icarus* **107**, 255–268.

Bottke, W. F., M. C. Nolan, R. Greenberg, and R. A. Kolvoord 1994b. Collisional lifetimes and impact statistics of near-Earth asteroids. In *Hazards Due to Comets and Asteroids* (T. Gehrels and M. S. Matthews, Eds.), pp. 337–357. Univ. of Arizona Press, Tucson.

Bottke, W. F., M. C. Nolan, H. J. Melosh, A. M. Vickery, and R. Greenberg 1996. Origin of the Spacewatch small Earth-approaching asteroids. *Icarus* **122**, 406–427.

Bottke, W. F., D. P. Rubincam, and J. A. Burns 1998. Consequences of the Yarkovsky effect on the orbital evolution of meteoroids: A prospectus. *Proc. Lunar Plant. Sci. Conf. 29th*, 1424–1425.

Burns, J. A. 1976. Elementary derivation of the perturbation equations of celestial mechanics. *Am. J. Phys.* **44**, 944–949.

Burns, J. A., and E. F. Tedesco 1979. Asteroid lightcurves—Results for rotations and shapes. In *Asteroids* (T. Gehrels, Ed.), pp. 494–527. Univ. of Arizona Press, Tucson.

Burns, J. A., P. L. Lamy, and S. Soter 1979. Radiation forces on small particles in the Solar System. *Icarus* **40**, 1–48.

Caffee, M. W., R. C. Reedy, J. N. Goswami, C. M. Hohenberg, and K. Marti 1988. Irradiation records in meteorites. In *Meteorites and the Early Solar System* (J. F. Kerridge and M. S. Matthews, Eds.), pp. 205–245. Univ. of Arizona Press, Tucson.

Cellino, A., V. Zappalà, and P. Farinella 1991. The size distribution of main-belt asteroids from IRAS data. *Mon. Not. R. Astron. Soc.* **253**, 561–574.

Chamberlin, A. B., D. K. Yeomans, P. W. Chodas, J. D. Giorgini, R. A. Jacobson, M. S. Keesey, J. H. Lieske, S. J. Ostro, E. M. Standish, and R. N. Wimberly 1997. JPL Solar System Dynamics WWW Site (http://ssd.jpl.nasa.gov/). *Bull. Am. Astron. Soc.* **29**, 2106.

Dobrovolskis, A. R., and J. A. Burns 1984. Angular momentum drain—A mechanism for despinning asteroids. *Icarus* **57**, 464–476.

Dohnanyi, J. W. 1969. Collisional models of asteroids and their debris. *J. Geophys. Res.* **74**, 2531–2554.

Doressoundiram, A., A. Cellino, M. Di Martino, F. Migliorini, and V. Zappalà 1998. The puzzling case of the Nysa–Polana family finally solved? *Bull. Am. Astron. Soc.* **30**, 505.

Duncan, M. J., and J. J. Lissauer 1997. Orbital stability of the uranian satellite system. *Icarus* **125**, 1–12.

Durda, D. D., R. Greenberg, and R. Jedicke 1998. Collisional models and scaling laws: A new interpretation of the shape of the main-belt asteroid size distribution. *Icarus* **135**, 431–440.

Farinella, P., and D. Vokrouhlický 1999. Semimajor axis mobility of asteroid fragments. *Science* **283**, 1507–1510.

Farinella, P., Ch. Froeschlé, Cl. Froeschlé, R. Gonczi, G. Hahn, A. Morbidelli, and G. B. Valsecchi 1994. Asteroids falling onto the Sun. *Nature* **371**, 315–317.

Farinella, P., R. Gonczi, Ch. Froeschlé, and Cl. Froeschlé 1993. The injection of asteroid fragments into resonances. *Icarus* **101**, 174–187.

Farinella, P., D. Vokrouhlický, and F. Barlier 1996. The rotation of LAGEOS and its long-term semimajor axis decay: A self-consistent solution. *J. Geophys. Res.* **101**, 17861–17872.

Farinella, P., D. Vokrouhlický, and W. K. Hartmann 1998. Meteorite delivery via Yarkovsky orbital drift. *Icarus* **132**, 378–387.

Farinella, P., D. Vokrouhlický, and W. K. Hartmann 1998b. Erratum: Meteorite delivery via Yarkovsky orbital drift. *Icarus* **134**, 347.

Gaffey, M. J., and S. L. Gilbert 1998. Asteroid 6 Hebe: The probable parent body of the H-Type ordinary chondrites and the IIE iron meteorites. *Meteor. Planet. Sci.* **33**, 1281–1295.

Gault, D. E., E. M. Shoemaker, and H. J. Moore 1963. Spray ejected from the lunar surface by meteoroid impact, NASA Tech. Note D-1767.

Geissler, P., J.-M. Petit, D. D. Durda, R. Greenberg, W. Bottke, M. Nolan, and J. Moore 1996. Erosion and ejecta reaccretion on 243 Ida and its moon. *Icarus* **120**, 140–157.

Gladman, B. 1997. Destination: Earth. Martian meteorite delivery. *Icarus* **130**, 228–246.

Gladman, B. J., J. A. Burns, M. Duncan, P. Lee, and H. F. Levison 1996. The exchange of impact ejecta between terrestrial planets. *Science* **271**, 1387–1392.

Gladman, B. J., F. Migliorini, A. Morbidelli, V. Zappalà, P. Michel, A. Cellino, C. Froeschlé, H. F. Levison, M. Bailey, and M. Duncan 1997. Dynamical lifetimes of objects injected into asteroid belt resonances. *Science* **277**, 197–201.

Goldreich, P. 1965, An explanation for the frequent occurrence of commensurable mean motions in the Solar System. *Mon. Not. R. Astron. Soc.* **130**, 159–181.

Graf, T., and K. Marti 1995. Collisional history of H chondrites. *J. Geophys. Res.* **100**, 221–247.

Greenberg, R. 1973. Evolution of satellite resonances by tidal dissipation. *Astron. J.* **78**, 338–346.

Greenberg, R., and C. R. Chapman 1983. Asteroids and meteorites—Parent bodies and delivered samples. *Icarus* **55**, 455–481.

Greenberg, R., W. K. Hartmann, C. R. Chapman, and J. F. Wacker 1978. Planetesimals to planets—Numerical simulation of collisional evolution. *Icarus* **35**, 1–26.

Hamilton, D. P. 1994. A comparison of Lorentz, planetary gravitational, and satellite gravitational resonances. *Icarus* **109**, 221–240.

Harris, A. W. 1996. The rotation rates of very small asteroids: Evidence for "rubble pile" structure. *Proc. Lunar Planet. Sci. Conf. 27th*, 493–494.

Hartmann, W. K., P. Farinella, D. Vokrouhlický, S. J. Weidenschilling, A. Morbidelli, F. Marzari, D. R. Davis, and E. Ryan 1999. Reviewing the Yarkovsky effect: New light on the delivery of stones and irons from the asteroid belt. *Meteor. Planet. Sci.* **34**, A161–A168.

Helfenstein, P., and 11 colleagues 1996. Galileo photometry of asteroid 243 Ida. *Icarus* **120**, 48–65.

Herzog, G. F., S. Vogt, A. Albrecht, S. Xue, D. Fink, J. Klein, R. Middleton, H. W. Weber, and L. Schultz 1997. Complex exposure histories for meteorites with "short" exposure ages. *Meteor. Planet. Sci.* **32**, 413–422.

Housen, K. R., K. A. Holsapple, and M. E. Voss 1999. Compaction as the origin of the unusual craters on the asteroid Mathilde. *Nature* **402**, 155–157.

Jedicke, R., and T. S. Metcalfe 1998. The orbital and absolute magnitude distributions of main belt asteroids. *Icarus* **131**, 245–260.

Lebofsky, L. A., and J. R. Spencer 1989. Radiometry and a thermal modeling of asteroids. In *Asteroids II* (R. P. Binzel, T. Gehrels, and M. S. Matthews, Eds.), pp. 128–147. Univ. of Arizona Press, Tucson.

Levison, H. F., and M. J. Duncan 1994. The long-term dynamical behavior of short-period comets. *Icarus* **108**, 18–36.

Malhotra, R. 1991. Tidal origin of the Laplace resonance and the resurfacing of Ganymede. *Icarus* **94**, 399–412.

Marti, K., and T. Graf 1992. Cosmic-ray exposure history of ordinary chondrites. *Ann. Rev. Earth Planet. Sci.* **20**, 221–243.

Michel, P., and G. B. Valsecchi 1996. Numerical experiments on the efficiency of second-order mixed-variable symplectic integrators of *N*-body problems. *Celest. Mech. Dynam. Astron.* **65**, 355–371.

Migliorini, F., A. Manara, F. Scaltriti, P. Farinella, A. Cellino, M. Di Martino 1997a. Surface properties of (6) Hebe: A posible parent body of ordinary chondrites. *Icarus* **128**, 104–113.

Migliorini, F., P. Michel, A. Morbidelli, D. Nesvorný, and V. Zappalà 1998. Origin of multikilometer Earth and Mars-crossing asteroids: A quantitative simulation. *Science* **281**, 2022–2024.

Migliorini, F., A. Morbidelli, V. Zappalà, B. J. Gladman, M. E. Bailey, and A. Cellino 1997b. Vesta fragments from ν_6 and 3:1 resonances: Implications for V-type NEAs and HED meteorites. *Meteor. Planet. Sci.* **32**, 903–916.

Morbidelli, A., and B. Gladman 1998. Orbital and temporal distributions of meteorites originating in the asteroid belt. *Meteor. Planet. Sci.* **33**, 999–1016.

Morbidelli, A., and M. Moons 1995. Numerical evidence on the chaotic nature of the 3/1 mean motion commensurability. *Icarus* **115**, 60–65.

Morbidelli, A., and D. Nesvorný 1999. Numerous weak resonances drive asteroids toward terrestrial planets' orbits. *Icarus* **139**, 295–308.

Morbidelli, A., R. Gonczi, Ch. Froeschlé, and P. Farinella 1994. Delivery of meteorites through the ν_6 secular resonance. *Astron. Astrophys.* **282**, 955–979.

Murray, N., M. Holman, and M. Potter 1998. On the origin of chaos in the asteroid belt. *Astron. J.* **116**, 2583–2589.

Nesvorný, D., and A. Morbidelli 1998. Three-body mean motion resonances and the chaotic structure of the asteroid belt. *Astron. J.* **116**, 3029–3037.

Ostro, S., and 19 colleagues 1999. Radar and optical observations of asteroid 1998 KY26. *Science* **285**, 557–559.

Peale, S. J. 1986. Orbital resonances, unusual configurations and exotic rotation states among planetary satellites. In *Satellites* (J. A. Burns and M. S. Matthews, Eds.), pp. 159–223. Univ. of Arizona Press, Tucson.

Peterson, C. 1976. A source mechanism for meteorites controlled by the Yarkovsky effect. *Icarus* **29**, 91–111.

Rabinowitz, D. L. 1994. The size and shape of the near-Earth asteroid belt. *Icarus* **111**, 364–377.

Rabinowitz, D. L., T. Gehrels, J. V. Scotti, R. S. McMillan, M. L. Perry, W. Wisniewski, S. M. Larson, E. S. Howell, and B. E. A. Mueller 1993. Evidence for a near-Earth asteroid belt. *Nature* **363**, 704–706.

Rubincam, D. P. 1987. LAGEOS orbit decay due to infrared radiation from Earth. *J. Geophys. Res.* **92**, 1287–1294.

Rubincam, D. P. 1988. Yarkovsky thermal drag on LAGEOS. *J. Geophys. Res.* **93**, 13805–13810.

Rubincam, D. P. 1995. Asteroid orbit evolution due to thermal drag. *J. Geophys. Res.* **100**, 1585–1594.

Rubincam, D. P. 1998. Yarkovsky thermal drag on small asteroids and Mars–Earth delivery. *J. Geophys. Res.* **103**, 1725–1732.

Schaffer, L., and J. A. Burns 1992. Lorentz resonances and the vertical structure of dusty rings—Analytical and numerical results. *Icarus* **96**, 65–84.

Spitale, J. N., and R. Greenberg 1999. Numerical investigation of the Yarkovsky effect: Mutiny on the high *e*'s. *Bull. Am. Astron. Soc.* **31**, 2405.

Stöffler, D., D. E. Gault, J. Wedekind, and G. Polkowski 1975. Experimental hypervelocity impact into quartz sand—Distribution and shock metamorphism of ejecta. *J. Geophys. Res.* **80**, 4062–4077.

Veverka, J., and 17 colleagues 1997. NEAR's flyby of 253 Mathilde: Images of a C asteroid. *Science* **278**, 2109–2114.

Vokrouhlický, D. 1998a. Diurnal Yarkovsky effect as a source of mobility of meter-sized asteroidal fragments, I: Linear theory. *Astron. Astrophys.* **335**, 1093–1100.

Vokrouhlický, D. 1998b. Diurnal Yarkovsky effect as a source of mobility of meter-sized asteroidal fragments, II: Non-sphericity effects. *Astron. Astrophys.* **338**, 353–363.

Vokrouhlický, D. 1999. A complete linear model for the Yarkovsky thermal force on spherical asteroid fragments. *Astron. Astrophys.* **344**, 362–366.

Vokrouhlický, D., and M. Brož 1999. An improved model of the seasonal Yarkovsky force for regolith-covered asteroid fragments. *Astron. Astrophys.* **350**, 1079–1084.

Vokrouhlický, D., and P. Farinella 1997. Recent progress in modeling the nongravitational forces affecting the LAGEOS orbit. *Adv. Space Res.* **19**, 1689–1693.

Vokrouhlický, D., and P. Farinella 1998a. The Yarkovsky seasonal effect on asteroidal fragments: A nonlinearized theory for the plane-parallel case. *Astron. J.* **116**, 2032–2041.

Vokrouhlický, D., and P. Farinella 1998b. Orbital evolution of asteroidal fragments into the ν_6 resonance via Yarkovsky effects. *Astron. Astrophys.* **335**, 351–362.

Vokrouhlický, D., and P. Farinella 2000. Delivery of stony meteorites from the asteroid belt: A dynamical–collisional Monte Carlo model *Nature*, submitted.

Ward, W. R. 1992. Long-term orbital and spin dynamics of Mars. In *Mars* (H. H. Kieffer, B. M. Jakosky, C. W. Snyder, and M. S. Matthews, Eds.), pp. 298–320. Univ. of Arizona Press, Tucson.

Weidenschilling, S. J., and A. A. Jackson 1993. Orbital resonances and Poynting–Robertson drag. *Icarus* **104**, 244–254.

Welten, K. C., L. Lindner, K. Van Der Borg, T. Loeken, P. Scherer, and L. Schultz 1997. Cosmic-ray exposure ages of diogenites and the recent collisional history of the HED parent body/bodies. *Meteor. Planet. Sci.* **32**, 891–902.

Wetherill, G. W. 1985. Asteroidal source of ordinary chondrites. *Meteoritics* **20**, 1–22.

Wetherill, G. W., and J. G. Williams 1979. Origin of differentiated meteorites. In *Origin and Distribution of the Elements* pp. 19–31. Pergamon, London.

Wisdom, J., and M. Holman 1991. Symplectic maps for the *N*-body problem *Astron. J.* **102**, 1528–1538.

Zappalà, V., P. Bendjoya, A. Cellino, P. Farinella, and C. Froeschlé 1995. Asteroid families: Search of a 12,487-asteroid sample using two different clustering techniques. *Icarus* **116**, 291–314.

Zappalà, V., A. Cellino, M. Di Martino, F. Migliorini, and P. Paolicchi 1997. Maria's family: Physical structure and possible implications for the origin of giant NEAs. *Icarus* **129**, 1–20.

Zappalà, V., A. Cellino, B. J. Gladman, S. Manley, and F. Migliorini 1998. Asteroid showers on Earth after family breakup events. *Icarus* **134**, 176–179.